



Publication Year	2017
Acceptance in OA @INAF	2020-07-22T05:36:04Z
Title	CoMaLit - V. Mass forecasting with proxies: method and application to weak lensing calibrated samples
Authors	Sereno, Mauro; ETTORI, STEFANO
DOI	10.1093/mnras/stx576
Handle	http://hdl.handle.net/20.500.12386/26556
Journal	MONTHLY NOTICES OF THE ROYAL ASTRONOMICAL SOCIETY
Number	468

CoMaLit – V. Mass forecasting with proxies: method and application to weak lensing calibrated samples

Mauro Sereno^{1,2★} and Stefano Ettori^{1,3}

¹INAF, Osservatorio Astronomico di Bologna, via Ranzani 1, I-40127 Bologna, Italy

²Dipartimento di Fisica e Astronomia, Alma Mater Studiorum – Università di Bologna, viale Bert Pichat 6/2, I-40127 Bologna, Italy

³INFN, Sezione di Bologna, viale Bert Pichat 6/2, I-40127 Bologna, Italy

Accepted 2017 March 6. Received 2017 March 5; in original form 2016 March 11

ABSTRACT

Mass measurements of astronomical objects are most wanted but still elusive. We need them to trace the formation and evolution of cosmic structure but we can get direct measurements only for a minority. This lack can be circumvented with a proxy and a scaling relation. The twofold goal of estimating the unbiased relation and finding the right proxy value to plug in can be hampered by systematics, selection effects, Eddington/Malmquist biases and time evolution. We present a Bayesian hierarchical method that deals with these issues. Masses to be predicted are treated as missing data in the regression and are estimated together with the scaling parameters. The calibration subsample with measured masses does not need to be representative of the full sample as far as it follows the same scaling relation. We apply the method to forecast weak lensing calibrated masses of the *Planck*, redMaPPer and MCXC clusters. *Planck* masses are biased low with respect to weak lensing calibrated masses, with a bias more pronounced for high-redshift clusters. MCXC masses are under-estimated by ~ 20 per cent, which may be ascribed to hydrostatic bias. Packages and catalogues are made available with the paper.

Key words: gravitational lensing: weak – methods: statistical – catalogues – galaxies: clusters: general – galaxies: clusters: intracluster medium.

1 INTRODUCTION

The accurate measurement of the mass of galaxy clusters is crucial to astrophysical investigation (Voit 2005; Limousin et al. 2013). Clusters of galaxies have a special place in the hierarchical scenario of structure formation in a universe dominated early by cold dark matter (CDM) and later by dark energy in the form of a cosmological constant. They are the most massive and latest objects to near viral equilibrium.

Theoretical models and numerical simulations of formation and evolution of cosmic structure are naturally expressed in terms of mass. Still, precise mass measurements are elusive and very difficult to get in the large samples detected by ongoing and future surveys (Laureijs et al. 2011; Pierre et al. 2016). The weak lensing (WL) mass, the X-ray mass relying on hydrostatic equilibrium (HE) or the mass based on galaxy dynamics can provide accurate estimates, but they can be either very expansive to get or reliable only for regular objects. WL and caustics masses are in principle independent of the equilibrium state of the clusters but are affected by their own systematics (Gardini et al. 2004; Meneghetti et al. 2010; Becker & Kravtsov 2011; Rasia et al. 2012; Svensmark, Wojtak &

Hansen 2015) and to date are available only in small samples (Rines et al. 2013; Applegate et al. 2014; Hoekstra et al. 2015; Okabe & Smith 2016; Umetsu et al. 2016).

The challenge is then to predict the mass given a cluster property (the proxy) that can be easily measured and that is strictly related to the mass, e.g. optical richness, X-ray luminosity, Sunyaev–Zel’dovich (SZ) flux. This requires the accurate calibration of the observable proxy through comparison with direct mass estimates (Andreon & Bergé 2012; Ettori 2013).

The main properties of galaxy clusters are expected to scale with the mass. If gravity is the dominant process, clusters are self-similar and scaling relations in form of scale-free power laws subsist among cluster properties (Kaiser 1986; Giodini et al. 2013). This picture is substantially confirmed by observations (Ettori 2013, 2015) and numerical simulations (Stanek et al. 2010; Fabjan et al. 2011; Angulo et al. 2012), which showed that intrinsic scatters around the median relations approximately follow a lognormal distribution. Deviations from the self-similar scheme come from non-gravitational processes, e.g. feedback and non-thermal processes, which can contribute significantly to the global energy budget (Maughan et al. 2012).

The best case scenario for a proxy is an observable that can be measured quickly and accurately and that can be given as input to a calibrating function whose output is the mass. This is not the

★ E-mail: mauro.sereno@unibo.it

scenario we live in. It is rare to measure the proxy with a level of accuracy such that we can consider the measurement uncertainty negligible. Furthermore, selection biases can make the measured proxy not representative of the nominal value we should use in the scaling relation. Finally, the knowledge of the scaling relation is uncertain too.

Scaling relations are not deterministic. We rather estimate the probability of a mass, given a proxy. The width of the probability density gives rise to an intrinsic scatter that limits the accuracy to which the mass can be estimated. Furthermore, the scaling relation is known with its own uncertainties. Significant efforts in the field of Bayesian hierarchical analysis have been pursued to efficiently derive scaling relations (D’Agostini 2005; Kelly 2007; Andreon & Bergé 2012; Maughan 2014; Mantz 2016; Sereno 2016).

This is the fifth in the CoMaLit (COmparing MAsses in LITerature) series of papers, wherein we have been applying Bayesian hierarchical methods with latent variables to comparative studies of masses and scaling relations. In the first paper of the series (Sereno & Ettori 2015b, CoMaLit-I), we considered the best route to calibrate scaling relations. We looked for systematic differences in WL and HE masses and we assessed the overall level of the intrinsic scatters. In the second paper of the series (Sereno, Ettori & Moscardini 2015, CoMaLit-II), we dealt with the measurements of scaling relations. We presented the Bayesian method and applied it to WL clusters with measured SZ flux. The third paper of the series (Sereno 2015, CoMaLit-III) introduced the Literature Catalogues of weak Lensing Clusters of galaxies (LC²), which we have been using to calibrate mass proxies. The fourth paper of the series (Sereno & Ettori 2015a, CoMaLit-IV) dealt with time-evolution and completeness. The scalings of optical richness, X-ray luminosity and galaxy velocity dispersion with mass were considered. Here, we deal with efficient mass prediction.

The present paper is structured as follows. In Section 2, we discuss the basics of a mass proxy. Sources of uncertainty, systematics and biases in mass prediction are listed in Section 3. The Bayesian hierarchical model is presented in Section 4. The calibration sample is introduced in Section 5. Mass forecast of *Planck*, redMaPPer or MCXC clusters is presented in Sections 6, 7 and 8, respectively. The comparison of WL calibrated masses is presented in Section 9. In Section 10, we discuss the reliability of heterogeneous calibration samples. Final considerations are given in Section 11. The Appendix details the implementation of the forecasting.

1.1 Conventions and notations

Throughout the series of papers, the frame-work cosmological model is the concordance flat Λ CDM universe with matter density parameter $\Omega_M = 1 - \Omega_\Lambda = 0.3$ and Hubble constant $H_0 = 70 \text{ km s}^{-1} \text{ Mpc}^{-1}$; $H(z)$ is the redshift-dependent Hubble parameter and $E_z \equiv H(z)/H_0$.

The redshift dependence T is expressed as F_z , which can be proportional to either E_z or $(1+z)$. D is either the luminosity or the angular diameter distance. The reference redshift is denoted as z_{ref} . F_z and D are normalized such that $F_z(z_{\text{ref}}) = 1$ and $D(z_{\text{ref}}) = 1$. In this paper, we set $F_z = E_z/E_z(z_{\text{ref}})$ with $z_{\text{ref}} = 0.01$.

O_Δ denotes a global property of the cluster measured within the radius that encloses a mean overdensity of Δ times the critical density at the cluster redshift, $\rho_{\text{cr}} = 3H(z)^2/(8\pi G)$. ‘log’ is the logarithm to base 10 and ‘ln’ is the natural logarithm.

Computations were performed with the R-package LIRA.¹ The full list of parameters considered in the most general regression scheme is presented in Table 1. The actual implementation for the cases studied in the present paper is detailed in Sections 4, 6, 7 and 8 and in the Appendix.

Products associated with this paper and the CoMaLit series are hosted at <http://pico.bo.astro.it/~sereno/CoMaLit/>.

2 EXPECTED MASS

Complexity, interactions and initial conditions can break self-similarity. We can try to model apparent deviations from determinism in terms of subtle effects. Differences from the self-similar model relating observables in X-ray and millimetre wave bands with the total mass can be efficiently expressed in a more complex picture in terms of the gas clumpiness, the gas mass fraction and the logarithmic slope of the thermal pressure profile (Ettori 2015).

Still, some inherent complexity can persist, observations may be not deep enough to assess faint features, and the model can get too intricate and unstable. One way to deal with such complexity is to introduce the concept of intrinsic scatter about a mean relation. We want to quantify the probability that a cluster has a mass, given a measured proxy, e.g. the luminosity, the richness and the temperature. This can be expressed in terms of a conditional probability.

Theoretical models (Kaiser 1986; Ettori 2013; Giodini et al. 2013), numerical simulations (Stanek et al. 2010; Fabjan et al. 2011; Angulo et al. 2012; Saro et al. 2013) and observations (Maughan 2007; Vikhlinin et al. 2009) favour power-law relations between cluster properties with a lognormal scatter around the mean. We can treat conveniently the problem in terms of the normal distribution if we work in the logarithmic space. Naming the covariate (i.e. the logarithm of the proxy) and the response (i.e. the logarithm of the mass) as X and Y , respectively, we can write

$$Y|X \sim \mathcal{N}(Y_X, \sigma_{Y|X}^2), \quad (1)$$

where \mathcal{N} is the normal distribution, the intrinsic scatter is quantified by the standard deviation $\sigma_{Y|X}$ and the mean is linearly related to the proxy X ,

$$Y_X = \alpha_{Y|X} + \beta_{Y|X} X + \gamma_{Y|X} T, \quad (2)$$

where $T(=\log F_z)$ embodies the redshift dependence.

Sources of uncertainty when we try to estimate Y , given X can come from the uncertainty associated with X , from uncertainties associated with the scaling relation and from uncertainties on the shape of the conditional probability.

3 ERRORS AND BIASES IN MODEL PREDICTION

Sources of uncertainty in mass prediction are variegated. In this section, we review some sources and discuss some ad hoc methods to deal with them under specific circumstances. These prescriptions can be useful, but they are not general and can fail in important cases of astronomical interest. We discuss them to illustrate the impact and the size of biases and errors which often plague the study of

¹The package LIRA (LInear Regression in Astronomy) is publicly available from the Comprehensive R Archive Network at <https://cran.r-project.org/web/packages/lira/index.html>. Beta versions can be downloaded from GitHub at <https://github.com/msereno/lira>. For further details, see Sereno (2016).

Table 1. List of the parameters of the regression scheme and their description. The variables Z is the covariate, X is a proxy of Z and Y is the response variable. Priors in square brackets can be set only as delta distributions. See the LIRA user manual for details.

Type	Meaning	Symbol	Code symbol	Default prior
<i>Y–Z scaling</i>				
$Y_Z = \alpha_{Y Z} + \beta_{Y Z}Z + \gamma_{Y Z}T + \delta_{Y Z}ZT$				
Conditional scaling relation	Intercept	$\alpha_{Y Z}$	alpha.YIZ	dunif
	Slope	$\beta_{Y Z}$	beta.YIZ	dt
	Time evolution	$\gamma_{Y Z}$	gamma.YIZ	dt
	Time tilt	$\delta_{Y Z}$	delta.YIZ	0
$Y_Z = \alpha_{Y Z, \text{knee}} + \beta_{Y Z, \text{knee}}Z + \gamma_{Y Z, \text{knee}}T + \delta_{Y Z, \text{knee}}ZT$				
Scaling relation before the break	Slope for $Z < Z_{\text{knee}}$	$\beta_{Y Z, \text{knee}}$	beta.YIZ.knee	beta.YIZ
	Time tilt for $Z < Z_{\text{knee}}$	$\delta_{Y Z, \text{knee}}$	delta.YIZ.knee	delta.YIZ
$f_{\text{knee}}(Z) = 1/(1 + \exp[(Z - Z_{\text{knee}})/l_{\text{knee}}])$				
Transition function	Break scale	Z_{knee}	Z.knee	dunif
	Break length	l_{knee}	l.knee	1e-04
<i>X–Z scaling</i>				
$X_Z = \alpha_{X Z} + \beta_{X Z}Z + \gamma_{X Z}T + \delta_{X Z}ZT$				
Proxy of the independent variable	Bias	$\alpha_{X Z}$	alpha.XIZ	0
	Slope	$\beta_{X Z}$	beta.XIZ	1
	Time evolution	$\gamma_{X Z}$	gamma.XIZ	0
	Time tilt	$\delta_{X Z}$	delta.XIZ	0
<i>Scatters</i>				
$\sigma_{Y Z} = [\sigma_{Y Z,0} + f_{\text{knee}}(Z)(\sigma_{Y Z,0,\text{knee}} - \sigma_{Y Z,0})]F_z^{\gamma_{\sigma_{Y Z},F_z}} D^{\gamma_{\sigma_{Y Z},D}}$				
Intrinsic scatter	Scatter at $z = z_{\text{ref}}$ for $Z \geq Z_{\text{knee}}$	$\sigma_{Y Z,0}$	sigma.YIZ.0	prec.dgamma
	Scatter at $z = z_{\text{ref}}$ for $Z < Z_{\text{knee}}$	$\sigma_{Y Z,0,\text{knee}}$	sigma.YIZ0.knee	sigma.YIZ.0
	Time evolution with F_z	$\gamma_{\sigma_{Y Z},F_z}$	gamma.sigma.YIZ.Fz	0
	Time evolution with D	$\gamma_{\sigma_{Y Z},D}$	gamma.sigma.YIZ.D	0
$\sigma_{X Z} = \sigma_{X Z,0}F_z^{\gamma_{\sigma_{X Z},F_z}} D^{\gamma_{\sigma_{X Z},D}}$				
Intrinsic scatter of the proxy	Scatter at $z = z_{\text{ref}}$	$\sigma_{X Z,0}$	sigma.XIZ.0	0
	Time evolution with F_z	$\gamma_{\sigma_{X Z},F_z}$	gamma.sigma.XIZ.Fz	0
	Time evolution with D	$\gamma_{\sigma_{X Z},D}$	gamma.sigma.XIZ.D	0
$\rho_{XY Z} = \rho_{XY Z,0}F_z^{\gamma_{\rho_{XY Z},F_z}} D^{\gamma_{\rho_{XY Z},D}}$				
Intrinsic scatter correlation	Correlation at $z = z_{\text{ref}}$	$\rho_{XY Z,0}$	rho.XYIZ.0	0
	Time evolution with F_z	$\gamma_{\rho_{XY Z},F_z}$	gamma.rho.XYIZ.Fz	0
	Time evolution with D	$\gamma_{\rho_{XY Z},D}$	gamma.rho.XYIZ.D	0
<i>Intrinsic distribution of the independent variable</i>				
$p(Z) \propto [\sum_k \pi_k \mathcal{N}(\mu_{Z,k}(z), \sigma_{Z,k}(z))] \text{erfc}[(\mu_{Z,\text{min}}(z) - Z)/\sigma_{Z,\text{min}}(z)/\sqrt{2}] \mathcal{U}(Z_{\text{max}} - Z)$				
Gaussian mixture	Number of components	n_{mix}	n.mixture	[1]
	Weights of the components	π_k	pi[k]	ddirch
	Maximum Z value (only for $n_{\text{mix}} = 1$)	Z_{max}	Z.max	$+\infty$
$\mu_{Z,k}(z) = \mu_{Z,0k} + \gamma_{\mu_{Z,k},F_z}T + \gamma_{\mu_{Z,k},D} \log D$				
Means of the Gaussian components	Mean of the first component at $z = z_{\text{ref}}$	$\mu_{Z,01}$	mu.Z.0	dunif
	Means of the additional components ($2 \leq k \leq n_{\text{mix}}$) at $z = z_{\text{ref}}$	$\mu_{Z,0k}$	mu.Z.0.mixture[k]	dunif
	Time evolution with F_z	$\gamma_{\mu_{Z,k},F_z}$	gamma.mu.Z.Fz	dt
	Time evolution with D	$\gamma_{\mu_{Z,k},D}$	gamma.mu.Z.D	dt
$\sigma_{Z,k}(z) = \sigma_{Z,0k}F_z^{\gamma_{\sigma_{Z,k},F_z}} D^{\gamma_{\sigma_{Z,k},D}}$				
Standard deviations of the Gaussian components	Deviation of the first component at $z = z_{\text{ref}}$	$\sigma_{Z,01}$	sigma.Z.0	prec.dgamma
	Deviations of the additional components ($2 \leq k \leq n_{\text{mix}}$) at $z = z_{\text{ref}}$	$\sigma_{Z,0k}$	sigma.Z.0.mixture[k]	prec.dgamma
	Time evolution with F_z	$\gamma_{\sigma_{Z,k},F_z}$	gamma.sigma.Z.Fz	0
	Time evolution with D	$\gamma_{\sigma_{Z,k},D}$	gamma.sigma.Z.D	0
$\mu_{Z,\text{min}}(z) = \mu_{Z,\text{min},0} + \gamma_{\mu_{Z,\text{min}},F_z}T + \gamma_{\mu_{Z,\text{min}},D} \log D$				
Minimum Z value (only for $n_{\text{mix}} = 1$)	Typical value at $z = z_{\text{ref}}$	$\mu_{Z,\text{min},0}$	mu.Z.min.0	$-\infty$
	Time evolution with F_z	$\gamma_{\mu_{Z,\text{min}},F_z}$	gamma.mu.Z.min.Fz	dt
	Time evolution with D	$\gamma_{\mu_{Z,\text{min}},D}$	gamma.mu.Z.min.D	dt
$\sigma_{Z,\text{min}}(z) = \sigma_{Z,\text{min},0}F_z^{\gamma_{\sigma_{Z,\text{min}},F_z}} D^{\gamma_{\sigma_{Z,\text{min}},D}}$				
Z_{min} dispersion	dispersion at $z = z_{\text{ref}}$	$\sigma_{Z,\text{min},0}$	sigma.Z.min.0	0
	Time evolution with F_z	$\gamma_{\sigma_{Z,\text{min}},F_z}$	gamma.sigma.Z.min.Fz	0
	Time evolution with D	$\gamma_{\sigma_{Z,\text{min}},D}$	gamma.sigma.Z.min.D	0

mass prediction and scaling relations. The general treatment of these effects in terms of a Bayesian hierarchical model, which should be used in the general case, is detailed in the following sections. In the most of this section, we identify the (logarithm of the) proxy with the covariate X and the (logarithm of the) mass with the response Y .

3.1 Intrinsic scatter

Since the scaling relation is scattered, an uncertainty related to the intrinsic dispersion $\sigma_{Y|X}$ is associated with the forecasting of the observable properties. This is usually one of the main sources of uncertainty. In the Bayesian treatment, we distinguish between a latent quantity that fits perfectly the scaling relation, Y_X in equations (1) and (2), and a scattered observable quantity, Y in equation (1), which is a scattered realization of the latent quantity Y_X . We associate the latent Y_X with the true mass and the observable Y with the WL mass.

3.2 Statistical measurement uncertainties in the proxy

The statistical uncertainty δ_x in the measurement process of the proxy X propagates to an uncertainty in the prediction,

$$\delta_Y = \beta_{Y|X} \delta_x. \quad (3)$$

This kind of uncertainty can be reduced with better measurements, but it cannot be eliminated.

3.3 Systematic measurement uncertainties in the proxy

Systematic uncertainties Δx in the proxy propagate as

$$\Delta_y = \beta_{Y|X} \Delta x. \quad (4)$$

Systematics can be related to the data-acquisition or to the statistical treatment. The former type can be eliminated only with a better understanding of the measurement process. In the following, we focus on the latter.

A bias can be defined as the difference between the average value of the observed quantity x and the true intrinsic value X for objects of the same class (Butkevich, Berdyugin & Teerikorpi 2005). If the quantity of interest is the absolute magnitude, biases are usually referred as Malmquist biases (Teerikorpi 1997).

These systematics can be turned on if the measurements are affected by some dispersion. This can be either the statistical uncertainty δ_x or the intrinsic scatter $\sigma_{Y|X}$. The formal treatment is the same. In the examples we detail next, we consider the statistical uncertainty.

The two biases we review have long been known and are usually named after Eddington or Malmquist. Still these biases are not always corrected for in analyses of scaling relations. The solutions that we discuss in the following apply only to specific cases. The general case must be addressed in a Bayesian framework, as detailed in Section 4.

3.3.1 Uneven distribution

The uneven distribution of the true variable X can be a source of bias in the presence of observational uncertainties δ_x . Similar considerations apply in case of intrinsic scatter rather than measurements errors (CoMaLit-I).

If the true number of objects in the range dX is greater than in adjacent ranges, on account of measurement errors more observations

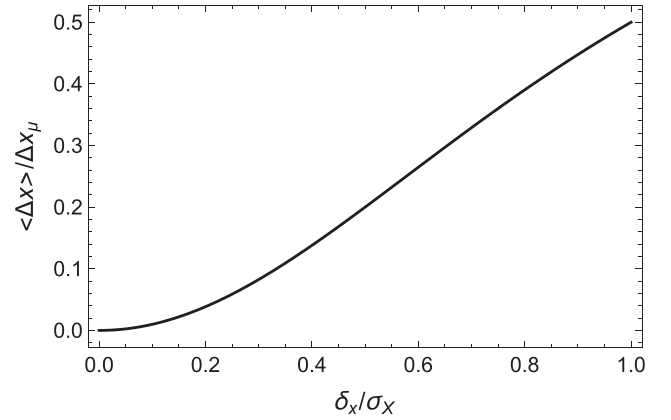


Figure 1. The bias due to a not-constant distribution of the independent variable, $p(X)$. Here, $p(X)$ is Gaussian. The bias $\langle \Delta x \rangle$, i.e. the difference between the average value of the observed quantity x and the true intrinsic value X for objects of the same class, is shown as a function of the measurement uncertainty δ_x . The bias is in units of Δx_μ , i.e. the distance of x from the mean of the distribution; the uncertainty δ_x is in units of the standard deviation of the distribution σ_X .

are scattered out of the range than into it (Eddington 1913, 1940; Jeffreys 1938). The distribution $p(x)$ of the observed variable x differs from the underlying true distribution of X . As a result, the average of the X values of a sample of objects with fixed x differs from the measured value, i.e. from x .

The average X value of an ensemble of objects with the same measured x is given by

$$\langle X \rangle(x) \propto \int X p(x, X) dX, \quad (5)$$

where $p(x, X)$ is the probability of x and X . We follow the treatment in appendix A of CoMaLit-I. We assume that the intrinsic distribution of true values is Gaussian

$$X \sim \mathcal{N}(\mu_X, \sigma_X^2), \quad (6)$$

and that the errors have a Gaussian distribution,

$$x|X \sim \mathcal{N}(X, \delta_x^2). \quad (7)$$

We assume that the uncertainty δ_x is constant. A simple application of Bayes' theorem shows that x and $X|x$ are normally distributed too (CoMaLit-I).

Given the above distributions, the mean X for a given x is (CoMaLit-I)

$$\langle X \rangle(x) = x + \langle \Delta x \rangle, \quad (8)$$

with a bias

$$\langle \Delta x \rangle = \frac{\mu_X - x}{1 + (\sigma_X / \delta_x)^2}. \quad (9)$$

For negative (positive) slopes of the underlying distribution, i.e. $x > (<) \mu_X$ for a Gaussian distribution, the measured x overestimates $\langle X \rangle(x)$, i.e. $\langle \Delta x \rangle < (>) 0$. The bias is more pronounced at the tails, being proportional to the distance of the observed value from the mean of the distribution, $\Delta x_\mu = \mu_X - x$. The bias $\langle \Delta x \rangle$ increases with the measurement error (see Fig. 1), and decreases with the dispersion of the distribution σ_X . For $\sigma_X = \delta_x$, $\langle \Delta x \rangle = \Delta x_\mu / 2$.

For a general distribution (Eddington 1940),

$$\langle \Delta x \rangle = \delta_x^2 \frac{d \ln p(x)}{dx}. \quad (10)$$

This kind of bias is analogous to the classical Malmquist bias (Malmquist 1922) and is classified as the magnitude-dependent Malmquist bias (Butkevich et al. 2005).

The distribution of corrected values computed according to equation (8) cannot be used for statistical inference without caveats (Eddington 1940). In fact, the procedure overcorrects the observational error. The distribution of the corrected values $x + \langle \Delta x \rangle$ deviates as far from the true distribution $p(X)$ in the direction of reduced spread as the observed distribution $p(x)$ does in the direction of increased dispersion.

3.3.2 Selection effects

A bias can show up if the conditional probability of the observed value x given the true value is skewed. Selection effects can distort the distribution of observed samples. Overluminous objects are overrepresented in flux-limited samples (Eddington 1914; Malmquist 1920).

Let us consider a sample selected with a hard cut in the observed value of the covariate. Only objects above a given threshold, $x > x_{\text{th}}$, are included. Our treatment is similar to Vikhlinin et al. (2009, appendix A.2) and to the so-called distance-dependent Malmquist bias (Butkevich et al. 2005). Due to selection effects, the conditional probability is truncated,

$$x|X \sim \mathcal{N}(X, \delta_x^2) \mathcal{U}(x - x_{\text{th}}), \quad (11)$$

where \mathcal{U} is the step function.

Differently from the bias discussed in Section 3.3.1, the selection bias does not come out due to the irregular distribution of the true variable. Even if the parent population of X is uniformly distributed, this bias can still be in place. However, due to the bias, the distribution of the observed X after selection is asymmetric.

The average bias of the detected objects is

$$\langle \Delta x \rangle = \int \int (x - X) p(x, X) dx dX. \quad (12)$$

Let us consider a single population with a given value of $X = X_0$, wherefore the distribution can be modelled with a Dirac delta function,

$$X \sim \delta_{\text{Dirac}}(X - X_0). \quad (13)$$

For a given X_0 , equation (12) simplifies as

$$\langle \Delta x \rangle = \int_{x_{\text{th}}}^{\infty} (x - X_0) p(x|X_0) dx. \quad (14)$$

We get

$$\langle \Delta x \rangle = \delta_x \frac{\exp[-(\Delta X_{\text{th}}/\delta_x)^2/2]}{\sqrt{\pi/2} \operatorname{erfc}[-\Delta X_{\text{th}}/(\sqrt{2}\delta_x)]}, \quad (15)$$

where $\Delta X_{\text{th}} = X_0 - x_{\text{th}}$ and ‘erfc’ is the complementary error function.

As shown in Fig. 2, the bias is prominent when the true value is deeply below the threshold, $X_0 \ll x_{\text{th}}$, when we expect that selected x s are just above x_{th} .

Note that the correction in equation (15) is written in terms of the unknown X_0 . In order to get the nominal X_0 given the measured x , the object-by-object correction should be performed by inversion,

$$x + \langle \Delta x \rangle(X_0) = X_0. \quad (16)$$

However, it seems common practice to compute the correction by computing the bias for x rather than for X_0 , i.e. $X_0 = x + \langle \Delta x \rangle(x)$

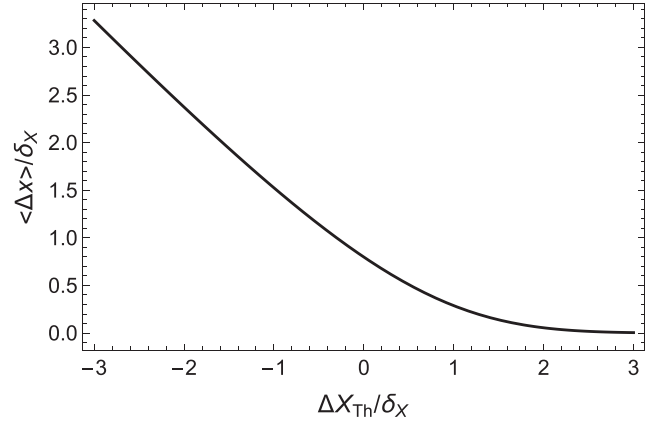


Figure 2. The bias due to selection effects when only objects with measured $x > x_{\text{th}}$ are retained in the sample. The bias $\langle \Delta x \rangle$, i.e. the difference between the average value of the observed x and the true intrinsic value X_0 , is shown as a function of the distance of the true value from the threshold, $\Delta X_{\text{th}} = X_0 - x_{\text{th}}$. The bias and ΔX_{th} are in units of the measurement uncertainty δ_x .

(Planck Collaboration XX 2014). This approximation can significantly underestimate the bias when the bias is large.

3.4 Scaling uncertainties

The degree of uncertainty on the scaling relation is a source of uncertainty in the mass forecast. Scaling parameters bring their own uncertainty. Even if the proxy is accurately known, the statistical errors on the scaling parameters propagate as

$$\delta_Y^2 = \delta_\alpha^2 + \delta_\beta^2 X^2 + 2\rho_{\alpha\beta} \delta_\alpha \delta_\beta X, \quad (17)$$

where $\rho_{\alpha\beta}$ is the uncertainty correlation factor.

The estimated slope and intercept are usually anticorrelated (Sereno & Ettori 2015a), which diminishes (augments) the combined error for positive (negative) X . This error associated with the scaling is proxy dependent and it can cause systematic effects.

3.5 Scattered response

Most of the scaling relations on the market are not universal. We can measure the galaxy richness of a cluster in terms of the number of red-sequence galaxies in some magnitude ranges, λ_{red} , or in terms of galaxies with similar photometric redshifts, $\lambda_{z_{\text{ph}}}$. Even if we manage to obtain the true $M-\lambda_{\text{red}}$ relation, we cannot use this relation straight away to measure the mass of a cluster with known $\lambda_{z_{\text{ph}}}$. In fact, $\lambda_{z_{\text{ph}}}$ is scattered with respect to λ_{red} .

This scatter $\sigma_{X_1|X_2}$, which may be unknown, can cause effects similar to measurement uncertainties in the proxy

$$\Delta_Y = \beta_{Y|X_2} \sigma_{X_1|X_2}, \quad (18)$$

and the related systematic effects discussed in Sections 3.3.1 and 3.3.2.

4 MODEL PREDICTION

The Bayesian hierarchical model developed in the CoMaLit series is already apt to model prediction. The approach is fully detailed in CoMaLit-IV and Sereno (2016). Here, we summarize the aspects relevant to model prediction.

Our data set consists of a sample of clusters with measured proxies \mathbf{x} . The corresponding masses \mathbf{y} may be either known, which constitute the calibration subsample, or unknown, which are the masses we want to predict.

4.1 General case

In the general CoMaLit scheme, we distinguish between the result of the measurement y_i of the i th cluster, the true value of the observable Y_i , i.e. the measurement we would get in absence of noise and which can differ from the actual measurement for the observational error $\delta_{y,i}$, and the $Y_{Z,i}$ variable, which exactly fits the scaling relation and can differ from Y_i for the intrinsic scatter. Similar notations hold for x_i , X_i and $X_{Z,i}$. Z is the underlying latent variable that X_Z and Y_Z are linearly related to.

The full probability density can be written as

$$p(\mathbf{x}, \mathbf{y}, \mathbf{X}, \mathbf{Y}, \mathbf{Z}, \boldsymbol{\pi}_{\text{SR}}, \boldsymbol{\pi}_{\text{Z}}) = \prod_i^{N_{\text{obs}}} \mathcal{L}_i(\mathbf{X}_i, \mathbf{Y}_i, \boldsymbol{\pi}_{\text{SR}}) P(\mathbf{Z}_i, \boldsymbol{\pi}_{\text{Z}}) \times P(\boldsymbol{\pi}_{\text{SR}}) P(\boldsymbol{\pi}_{\text{Z}}), \quad (19)$$

where $\boldsymbol{\pi}_{\text{SR}}$ and $\boldsymbol{\pi}_{\text{Z}}$ are the meta-parameters characterizing the scaling relation and the intrinsic distribution of the independent variable, respectively. $P(\boldsymbol{\pi}_{\text{SR}})$ and $P(\boldsymbol{\pi}_{\text{Z}})$ are the prior distributions. N_{obs} is the number of clusters in the sample and the independent variable \mathbf{Z}_i is drawn from the probability distribution of the selected clusters, $P(\mathbf{Z}, \boldsymbol{\pi}_{\text{Z}})$.

The likelihood for the i th cluster can be expressed as

$$\mathcal{L}_i = P(\mathbf{x}_i, \mathbf{y}_i | \mathbf{X}_i, \mathbf{Y}_i) P(\mathbf{X}_i, \mathbf{Y}_i | \mathbf{Z}_i, \boldsymbol{\pi}_{\text{SR}}), \quad (20)$$

where $P(\mathbf{x}_i, \mathbf{y}_i | \mathbf{X}_i, \mathbf{Y}_i)$ is the joint conditional probability of the measurements given the true values and $P(\mathbf{X}_i, \mathbf{Y}_i | \mathbf{Z}_i, \boldsymbol{\pi}_{\text{SR}})$ is the probability of the true values given the latent variable \mathbf{Z} .

The expressions of the full probability density in equation (19) and the likelihood in equation (20) are general. The form of the conditional probabilities $P(\mathbf{x}_i, \mathbf{y}_i | \mathbf{X}_i, \mathbf{Y}_i)$ and $P(\mathbf{X}_i, \mathbf{Y}_i | \mathbf{Z}_i, \boldsymbol{\pi}_{\text{SR}})$ can change in the presence of selection effects that can truncate or curtail the distributions. As a result, the sampled population of the covariate, which models the distribution of the selected objects, differs from the parent population of all objects before selection.

In the CoMaLit approach, we model these probabilities as bivariate normal distributions to account for correlated measurement errors and correlated scatters. Distributions can be truncated to account for selection effects. We refer to [CoMaLit-IV](#) for full details.

For linear scaling and in absence of biases, the expected value of Y given Z is

$$Y_Z = \alpha_{Y|Z} + \beta_{Y|Z} Z + \gamma_{Y|Z} T, \quad (21)$$

where T expresses the redshift dependence and it is assumed to be known. A similar relation holds between X_Z and Z .

4.2 Unscattered proxy

We can then distinguish different cases in astronomy. In forecasting, we may want to estimate Y given X , which we can directly measure. For scaling relations, we may be interested either in the relation between Y and Z , which is the latent variable that ideally fits a scaling relation, or in the relation between Y and X . In the following sections, we will focus on forecasting, i.e. Y given X .

When we are interested in forecasting, we can usually deal with a simplified scheme. If we want to predict the mass corresponding to the actual realization of the proxy, we can consider the proxy as

unscattered. The proxy is still affected by measurement uncertainties but, in this simplified forecasting scheme, we do not have to consider the conditional scatter of the independent variable. In the CoMaLit formalism, we can now identify X with Z , i.e. X is not affected by intrinsic scatter with respect to Z .

For mass prediction, y_i is the (logarithm of the) measured mass, e.g. the WL mass, Y_i is the true WL mass and the $Y_{Z,i}$ is the true mass. We usually want to estimate $Y_{Z,i}$, i.e. we are mostly interested in the true mass rather than in the WL mass. The measured mass proxy is x_i , whereas the proxy we would measure in absence of noise is X_i . The full probability density in equation (19) reduces to

$$p(\mathbf{x}, \mathbf{y}, \mathbf{X}, \mathbf{Y}, \boldsymbol{\pi}_{\text{SR}}, \boldsymbol{\pi}_{\text{X}}) = \prod_i^{N_{\text{obs}}} \mathcal{L}_i(\mathbf{X}_i, \mathbf{Y}_i, \boldsymbol{\pi}_{\text{SR}}) P(\mathbf{X}_i, \boldsymbol{\pi}_{\text{X}}) \times P(\boldsymbol{\pi}_{\text{SR}}) P(\boldsymbol{\pi}_{\text{X}}), \quad (22)$$

where the likelihood can be written as

$$\mathcal{L}_i = P(\mathbf{x}_i, \mathbf{y}_i | \mathbf{X}_i, \mathbf{Y}_i) P(\mathbf{Y}_i | \mathbf{X}_i, \boldsymbol{\pi}_{\text{SR}}). \quad (23)$$

The intrinsic distribution of the covariate can be written as $P(\mathbf{X}_i | \boldsymbol{\pi}_{\text{X}})$ rather than in terms of Z , which is now an unnecessary variable.

Here, we are limiting our analysis only to the N_{obs} selected clusters that are included in the sample. Because of the catalogue selection method, the sample only includes N_{obs} clusters out of the possible N_{tot} sources located within the survey area. N_{tot} is unknown and should thus also be treated as a parameter of the statistical model. The data likelihood should be written as a product running over all the N_{tot} clusters, either detected or missed. Here, N_{tot} is expressed in terms of the theoretical halo mass function, whereas the selection function enters as the probability of including a source with a given \mathbf{x} and \mathbf{y} .

However, when the sample selection function is dependent of the observed \mathbf{x} only, i.e. it does not depend on \mathbf{y} , and the measurement errors on \mathbf{y} and \mathbf{x} are statistically independent, the terms in the data-likelihood including \mathbf{y} and \mathbf{Y} of the $N_{\text{tot}} - N_{\text{obs}}$ missing sources can be integrated over (Kelly 2007). This is actually the case we deal with in the following sections. We refer to Kelly (2007) for full details.

As a result, the final data likelihood can be written in terms of the N_{obs} detected clusters only, with the caveat that $p(\mathbf{X})$ only models the distribution of the clusters that have been included in the sample. This simplification is expressed in equation (23). Because we are primarily interested in inference on regression parameters and unknown masses of the detected clusters, we can omit from the likelihood the lasting terms depending on N_{tot} .

This approach is workable only if we are not interested in cosmology and cluster abundance, since N_{tot} embodies the cosmological information.

If the mass y_i is measured and known, the variables Y_i and $Y_{Z,i}$ are constrained in two ways. On one side, the response is anchored to the measurement result through $P(\mathbf{x}_i, \mathbf{y}_i | \mathbf{X}_i, \mathbf{Y}_i)$, where we are considering possibly correlated measurements. On the other side, Y_i has to fit the scaling relation through $P(\mathbf{Y}_i | \mathbf{X}_i, \boldsymbol{\pi}_{\text{SR}})$. This double requirement allows us to estimate at the same time X , Y , Y_Z and the scaling relation. Whereas y is the direct output of the measurement process, Y is a refined estimate of the WL mass that exploits the information about linearity.

If the data are missing, Y is determined solely by the scaling relation. The measured x_i and the missing y_i are uncorrelated,

$$P(\mathbf{x}_i, \mathbf{y}_i | \mathbf{X}_i, \mathbf{Y}_i) = P(\mathbf{x}_i | \mathbf{X}_i) P(\mathbf{y}_i | \mathbf{Y}_i). \quad (24)$$

The true WL mass Y_i and the true mass $Y_{Z,i}$ are now determined by the scaling $P(Y_i|X_i, \pi_{SR})$. The constraint from x_i still actively participates in the inference of the unbiased intrinsic distribution $P(X)$.

The scaling parameters are mainly determined by the data with measured y . However, the full distribution $p(x)$ helps to constrain the covariate distribution $p(X)$, which is crucial for bias correction.

In the CoMaLit approach, we can model the distribution of the covariate $P(Z)$ as a Gaussian distribution, a mixture of Gaussian distributions, or a truncated Gaussian distribution. The truncation can be hard or smooth, when the Gaussian is multiplied by a complementary error function [see [CoMaLit-IV](#) and Sereno (2016) for details]. All the parameters entering the covariate distribution can be redshift evolving. This set of distributions can properly model an ample range of physical cases. The most basic case, i.e. a simple Gaussian function, is flexible enough to cover most of the sensible cases.

The described Bayesian hierarchical model can be useful for mass estimates even if the data set is complete with no missing measurement. In fact, the regression determines both the WL calibrated mass Y and the true mass Y_Z . This can be particularly useful in the presence of selection biases. On the other hand, if the WL measurement is missing, the regression can estimate the mass based on the global scaling.

Scaling parameters and missing data are determined at the same time during the regression. The Bayesian method accounts for heteroscedastic and possibly correlated measurement errors, intrinsic scatter, time evolution, distribution of the independent variable and selection effects in the covariate or the response variable. In the same way, the procedure provides corrected estimates of the proxy X too.

The Bayesian treatment deals with the scaling relation and the forecasting at the same time and the predicted masses do not suffer from the issues raised in Section 3. Systematics are accounted for whereas all statistical sources of uncertainty are included in the uncertainty budget.

The CoMaLit approach fully implements the described scheme by modelling the conditional probabilities with redshift evolving normal distributions. Gaussian distributions can be truncated or skewed to account for selection effects. The priors are fully customizable.

The method is implemented in `LIRA`, and it does not formally distinguish between data and parameters. Missing data values are treated as parameters to be estimated. If a node, i.e. a statistical relation $P(y_i|Y_i)$, contains a missing value for the unobserved element ($y_i = \text{NA}$), the posterior distribution for the node can be sampled. The resulting samples at the NA locations in the response vector are samples from the posterior predictive distribution and can be summarized just like model parameters.

5 CALIBRATION SAMPLE

Scaling relations to be used in mass forecasting have to be assessed through a subsample of clusters with well-measured masses. WL masses are arguably the more reliable mass estimates ([CoMaLit-I](#)). They do not depend on the dynamical state of the cluster (as far as the mass distribution is well modelled), are nearly unbiased, and with a quite small intrinsic scatter of ~ 10 per cent. These features make WL masses optimal for the calibration of mass proxies (Becker & Kravtsov 2011; Rasia et al. 2012; Sereno & Ettori 2015b).

As calibration sample, we considered the Literature Catalogues of weak Lensing Clusters of galaxies (LC²), the largest compilation of

Table 2. Characteristics of the considered WL samples. Column 1: name. Column 2: number of clusters, N_{cl} . Columns 3 and 4: typical redshift and dispersion. Columns 5 and 6: typical mass and dispersion. Column 7: main reference. Typical values and dispersions are computed as bi-weighted estimators. Masses are in units of $10^{14} M_{\odot}$.

Sample	N_{cl}	z	σ_z	M_{500}	σ_M	Reference
LC ² -single	506	0.31	0.18	5.0	4.5	Sereno (2015)
CCCP	54	0.24	0.10	7.7	4.2	Hoekstra et al. (2015)
WtG	51	0.38	0.14	10.5	5.1	Applegate et al. (2014)
LoCuSS	50	0.23	0.04	6.5	3.1	Okabe & Smith (2016)
CLASH	20	0.38	0.13	10.0	4.0	Umetsu et al. (2016)

WL masses to date² ([CoMaLit-III](#)). LC² are standardized catalogues of galaxy clusters with measured WL mass retrieved from literature. The latest compilation lists 879 WL analyses of clusters and groups with measured redshift and mass from 81 bibliographic sources. The catalogues report coordinates, redshift, WL masses to overdensities of 2500, 500, 200, and to the virial radius and spherical WL masses within 0.5, 1.0 and 1.5 Mpc.

For our main analysis, we considered the catalogue of unique entries LC²-single. For clusters with multiple analyses, the WL study exploiting the deepest observations and the most complete multiband coverage was picked out. This criterion usually selects the most recent analysis, e.g. either the CLASH (Cluster Lensing And Supernova survey with Hubble; Umetsu et al. 2016) or the WtG (Weighing the Giants; Applegate et al. 2014) clusters.

The catalogue spans a large interval in redshift $0.02 \lesssim z \lesssim 1.5$ and mass $0.03 \lesssim M_{500}/(10^{14} M_{\odot}) \lesssim 30$. Main properties are summarized in Table 2. We refer to [CoMaLit-III](#) for a detailed discussion of the catalogue properties. For testing and comparison, we also considered smaller but homogeneous samples (see Table 2).

6 THE PLANCK SZ CATALOGUE

The second *Planck* Catalogue of Sunyaev–Zel’dovich Sources (PSZ2; Planck Collaboration XXVII 2016a) is the largest SZ-selected sample of galaxy clusters yet produced and the deepest all-sky catalogue of galaxy clusters. The second release of the catalogue contains 1653 sources detected with a SNR (signal-to-noise ratio) above 4.5 from the 29 months full-mission data, of which 1203 are confirmed clusters with counterparts identified in external optical or X-ray samples or by dedicated follow-ups.

As selection pipeline, we considered the Matched Multi-Filter method MMF3, which identified 1271 candidates. The redshift determination is available for 926 clusters. The catalogue spans a broad nominal mass range from $M_{500} \sim 0.1$ to $16 \times 10^{14} M_{\odot}$. The median redshift is $z \sim 0.22$. We provide WL calibrated mass estimates for the subsample of MMF3 detections with measured redshift.

6.1 Planck mass prediction

Let us summarize the mass calibration adopted by the *Planck* team (Planck Collaboration XX 2014). The *Planck* team estimated the mass of the detected clusters with known redshift assuming the best-fitting scaling relation between M_{500} and Y_{500} , i.e. the spherically integrated Compton parameter within a sphere of radius

² The catalogues are available at <http://pico.bo.astro.it/~sereno/CoMaLit/LC2/>

r_{500} . The scaling between mass and SZ flux was modelled as (Planck Collaboration XX 2014)

$$E_z^{-2/3} \left[\frac{D_z^2 Y_{500}}{10^{-4} \text{ Mpc}^2} \right] = 10^\alpha \left[\frac{M_{500}}{M_{\text{pivot}}} \right]^\beta, \quad (25)$$

where the redshift evolution is set to self-similarity, D_z is the angular diameter distance to the cluster, $M_{\text{pivot}} = 6 \times 10^{14} M_\odot$, $\alpha = -0.186 \pm 0.011$ and $\beta = 1.79 \pm 0.06$.

The Y_{500} – M_{500} relation was determined through multiple steps (Planck Collaboration XX 2014). The first step involved Y_X , i.e. the X-ray analogue of Y_{500} defined as the product of the gas mass within r_{500} and the spectroscopic temperature outside the core (Kravtsov, Vikhlinin & Nagai 2006).³ The local Y_X – $M_{\text{HE}, 500}$ relation was estimated in a sample of 20 relatively relaxed local clusters (Arnaud et al. 2010). This calibration sample is not representative of the full *Planck* catalogue. Masses estimated through this scaling relation are denoted as $M_{500}^{Y_X}$.

Secondly, the Y_{500} – $M_{500}^{Y_X}$ relation was computed for 71 detections from the *Planck* cosmological sample with good quality *XMM*–*Newton* observations. The SZ fluxes were re-estimated within a sphere of radius $r_{500}^{Y_X}$, centred on the position of the X-ray peak.

The Y_{500} – M_{500} relation (see equation 25) was finally used as a prior that cuts through the parameter likelihood contours of the SZ observables to estimate the mass. This mass should equal the hydrostatic mass expected for a cluster consistent with the assumed scaling relation, at a given redshift and given the *Planck* posterior information. In the *Planck* papers, the masses estimated through the scaling relation are denoted as M_{SZ} or $M_{500}^{Y_Z}$.

The errors quoted in the PSZ2 catalogue are the 68 per cent confidence statistical errors and are based on the measurement uncertainties only. They do not include the statistical errors on the scaling relation, the intrinsic scatter in the relation, or systematic errors in data selection for the scaling relation fit.

A bias b_{SZ} can still persist in the HE mass measurements, $M_{\text{HE}, 500} = (1 - b_{\text{SZ}})M_{500}$ (Planck Collaboration XX 2014). Based on a suite of numerical simulations (Battaglia et al. 2012; Kay et al. 2012), the *Planck* team estimated $b_{\text{SZ}} = 0.2_{-0.2}^{+0.1}$.

6.2 *Planck* masses versus WL masses

The level of bias of the *Planck*-derived masses can be assessed by direct comparison with WL masses. We identified a WL cluster as a counterpart of a PSZ2 candidate if their redshifts differ for less than $\Delta z = 0.01$ and their angular separation in the sky does not exceed 3/2 times the SZ position uncertainty.⁴ We also excluded cluster pairs separated by more than 10 arcmin. In case of multiple matches, we retained the candidate that was the closest in the sky.

The estimate of the bias is strongly dependent on the methodology and on the calibration sample. According to the sample selection criteria, corrections for Eddington bias have to be applied (CoMaLit-I, Battaglia et al. 2016). The usual approach, which we followed to ease comparison with previous results, is to consider only the subsample of SZ detected clusters with WL observations.

Alternatively, you can consider *Planck* measurements as follow-up observations of the WL sample and then account for non-

Table 3. Bias of the *Planck* SZ masses derived from various calibration samples of WL masses. Column 1: sample name. Column 2: number of WL clusters, N_{cl} , detected by *Planck* with the MMF3 algorithm. Columns 3 and 4: typical redshift and dispersion. Columns 5 and 6: typical WL mass and dispersion in units of $10^{14} M_\odot$. Column 7: bias $b_{\text{SZ}} = \ln(M_{\text{SZ}}/M_{\text{WL}})$. Typical values and dispersions are computed as bi-weighted estimators.

Sample	N_{cl}	z	σ_z	M_{500}	$\sigma_{M_{500}}$	b_{SZ}
LC ² -single	135	0.24	0.14	7.8	4.8	-0.25 ± 0.04
CCCP	35	0.23	0.07	8.5	3.8	-0.22 ± 0.07
CLASH	13	0.37	0.13	11.3	3.3	-0.39 ± 0.08
LoCuSS	38	0.23	0.04	7.5	2.8	-0.18 ± 0.05
WtG	37	0.36	0.13	11.5	5.2	-0.43 ± 0.06

detections by setting the SZ signal of non-detected clusters to values corresponding to a multiple of the average SZ error (Battaglia et al. 2016).

For a detailed discussion of the bias and of recent measurements, we refer to CoMaLit-II. Here, we only update the results to the latest catalogue releases. To assess the effect of the calibration sample, we measured the bias for *Planck* clusters with estimated WL masses. Following the approach detailed in CoMaLit-I, the bias was estimated by fitting the relation⁵

$$\ln(M_{\text{SZ}}) = b_{\text{SZ}} + \ln(M_{\text{WL}}). \quad (26)$$

We considered both observational uncertainties and intrinsic scatters in the two mass estimates. The regression was performed with LIRA. We found $b_{\text{SZ}} = -0.25 \pm 0.14$ (see Table 3).

Our result is consistent with previous estimates based on WL comparison. von der Linden et al. (2014) found a large bias of $b_{\text{SZ}} = 0.30 \pm 0.06$ in the WtG sample. Planck Collaboration XXIV (2016c) found a bias of $b_{\text{SZ}} = -0.32 \pm 0.07$ for the WtG sample, $b_{\text{SZ}} = -0.22 \pm 0.09$ for the CCCP (Canadian Cluster Comparison Project, Hoekstra et al. 2015) sample and $b_{\text{SZ}} \sim 1$ from CMB (Cosmic Microwave Background) lensing. Smith et al. (2016) found that the mean bias with respect to the LoCuSS (Local Cluster Substructure Survey, Okabe & Smith 2016) sample is $b_{\text{SZ}} = -0.05 \pm 0.04$.

6.3 WL calibrated masses

Following the method described in Section 4.2, we derived the WL calibrated masses for all the MMF3 *Planck* clusters with measured redshift. The calibration sample consists of 135 clusters with WL measurements (see Table 3). The catalogue of masses is released with the paper, and it is also available at <http://pico.bo.astro.it/~sereno/CoMaLit>. An extract of the catalogue is presented in Table 4. Here and in the following, we denote direct WL mass measurements, i.e. the original masses measured with WL analyses and not reprocessed through the Bayesian method, as M_{WL} . Masses from the LC²-single catalogue can be alternatively denoted as M_{WL} or M_{LC^2} . We denote weak lensing calibrated (WLC) masses, i.e. mass estimates based on the scaling relation and WL measurement, if any, as M_{WLC} .

³ The X-ray quantity Y_X defined in this section should not be confused with the variable Y_X used in the Bayesian model.

⁴ The positional accuracy quoted in the MMF3 algorithm catalogue is defined as the 95 per cent confidence interval of the distribution of radial displacement (Planck Collaboration XXVII 2016a).

⁵ The bias b_{SZ} in equation (26) is defined as $b_{\text{SZ}} = \ln M_{\text{SZ}} - \ln M_{\text{WL}}$, whereas in the *Planck* papers the bias is defined as $b_{\text{SZ}} = M_{\text{SZ}}/M_{500} - 1$. Since b_{SZ} is small and the WL mass is a low scatter proxy of the true mass, the two definitions are approximately interchangeable.

Table 4. The first 10 entries of the catalogue of WL calibrated masses of the PSZ2 clusters, `HFI_PCCS_SZ-MMF3_R2.08_MWLC.DAT`. The full catalogue is available in electronic form. Column 1: index of detection. Column 2: name of PSZ2 detection. Columns 3 and 4: right ascension and declination (J2000) of the *Planck* detection. Column 5: redshift of the cluster; Columns 6 and 7: WL calibrated mass M_{WLc} and associated error. Columns 8 and 9: WL mass of the LC²-single counterpart, M_{LC2} and associated error. Columns 10 and 11: SZ mass proxy M_{SZ} and associated error, as from the *Planck* catalogue. Masses are within r_{500} and they are in units of $10^{14} M_{\odot}$.

Index	Name	RA	Dec	z	MWLC	MWLC_ERR	MLC2	MLC2_ERR	MSZ	MSZ_ERR
1	PSZ2_G000.04+45.13	229.1905	−1.0172	0.1198	4.175	0.512	NA	NA	3.776	0.361
2	PSZ2_G000.13+78.04	203.5587	20.2560	0.1710	5.897	0.478	NA	NA	5.121	0.335
3	PSZ2_G000.40−41.86	316.0845	−41.3542	0.1651	5.593	0.473	9.387	2.485	4.785	0.338
4	PSZ2_G000.77−35.69	307.9728	−40.5987	0.3416	8.192	0.883	NA	NA	6.310	0.599
6	PSZ2_G002.08−68.28	349.6324	−36.3326	0.1400	2.681	0.737	NA	NA	2.789	0.417
8	PSZ2_G002.77−56.16	334.6595	−38.8794	0.1411	5.006	0.437	5.731	1.673	4.389	0.300
9	PSZ2_G002.82+39.23	235.0152	−3.2851	0.1533	6.221	0.616	9.100	1.950	5.490	0.495
11	PSZ2_G003.21−76.04	358.3512	−33.2932	−1	NA	NA	NA	NA	NA	NA
12	PSZ2_G003.91−42.03	316.4675	−38.7532	0.1521	5.151	0.482	NA	NA	4.525	0.350
13	PSZ2_G003.93−59.41	338.6081	−37.7413	0.1510	7.471	0.496	5.467	2.004	6.652	0.257

6.3.1 The proxy

Scaling relations referring to an overdensity radius can be ambiguous. If we know the overdensity radius, which we need to measure the proxy, we already know the mass by definition. Here, we favour a more direct approach wherein the proxy is measured in an effective overdensity radius $r_{\Delta, \text{proxy}}$, whereas the mass is measured within the true overdensity radius r_{Δ} . The effective $r_{\Delta, \text{proxy}}$ can be estimated with a scaling relation or can be a fixed length. These choices simplify the proxy, whose measurement is then not correlated to the mass.

As a proxy, we considered the spherically integrated Compton parameter Y_{500} .⁶ The effective $r_{500, \text{proxy}}$ was determined by the *Planck* team through the Y_{500} – M_{500} relation (see Section 6.1).

The Compton parameter Y_{500} probes a large region and it is only marginally dependent on the integration radius. We tested that its estimate varies negligibly if we re-derived it from the likelihood under a WL prior, i.e. adopting r_{500} from the WL analysis, or after re-centring (CoMaLit-II).

In the CoMaLit notation, we can identify x with the measured proxy,

$$x = \log(10^4 D_z^2 Y_{500} / E_z^{2/3} / \text{Mpc}^2). \quad (27)$$

6.3.2 Selection effects

The PSZ2 sample is selected by the SZ properties. By approximating $\text{SNR} \sim Y_{500} / \delta Y_{500}$, the limiting flux of the i th *Planck* cluster is obtained by multiplying the minimum SNR by the uncertainty on the integrated Compton parameter (CoMaLit-II). In terms of SNR,

$$x_{\text{th},i} = x_i + \log(\text{SNR}_{\text{th}} / \text{SNR}_i), \quad (28)$$

where the limiting signal-to-noise ratio is $\text{SNR}_{\text{th}} = 4.5$. The selection threshold affects the conditional probability of the measurements, which we model as in equation (11),

$$x_i | X_i \sim \mathcal{N}(X_i, \delta_{x,i}^2) \mathcal{U}(x_i - x_{\text{th},i}). \quad (29)$$

⁶ The values of Y_{500} were retrieved from the third extension HDU (Header Data Unit) of the individual MMF3 algorithm catalogue. Practically, we translated the quoted masses to Y_{500} by means of the scaling relation. We tested that this estimate is fully compatible with the SZ flux derived by us from the likelihood tabulated function applying the scaling relation prior.

We refer the interested readers to CoMaLit-IV and Sereno (2016) for full details.

Since the selection thresholds are point dependent, there is no steep lower bound in the distribution of the observed SZ fluxes. Furthermore, the distribution is smoothed by observational errors. As a result, the distribution of the covariate is regular and can be well approximated as a redshift-evolving Gaussian function. We refer to CoMaLit-II and CoMaLit-IV for details.

We considered the full PSZ2 and did not apply selection procedures based on the WL properties. Masses of clusters without WL estimates were treated as missing data. Clusters with known WL mass effectively sample the massive end of the PSZ2 catalogue (CoMaLit-II). Under the assumption that there are no breaks at the lower mass end or at high redshifts, the calibration sample follows the same scaling relation of the full sample and it is affected by the same intrinsic scatter. As far as we model the distribution of the proxies of the full sample, selection effects related to the WL measurements can be neglected if the scatter and the scaling of the WL clusters are representative of the full PSZ2 sample.

6.3.3 The masses

The response is the mass. We denote

$$y = \log(M_{\text{LC2},500} / 10^{14} / M_{\odot}), \quad (30)$$

$$Y_X = \log(M_{\text{WLc},500} / 10^{14} / M_{\odot}). \quad (31)$$

We linearly fitted the proxies and the responses. The fitting procedure retrieves at the same time the masses and the scaling relation.

The scattered scaling relation can be expressed as

$$Y \sim \mathcal{N}(Y_X = \alpha_{Y|X} + \beta_{Y|X} X + \gamma_{Y|X} T, \sigma_{Y|X}^2). \quad (32)$$

The parameter $\gamma_{Y|X}$ accounts for the redshift-evolution of the relation. Since the proxies are rescaled by $E_z^{2/3}$ (see equation 27), $\gamma_{Y|X} = 0$ means self-similar evolution.

Since the intrinsic scatter of the scaling is expected to be log-normal, we fitted the logarithms. When needed, here and in the following, we assumed relations derived for the lognormal distribution to go from $\langle \log y \rangle$ to $\log \langle y \rangle$ (and similarly for other variables).

The results of the regression are plotted in Fig. 3. As scaling parameters, we found $\alpha_{Y|X} = 0.89 \pm 0.04$, $\beta_{Y|X} = 0.54 \pm 0.06$, $\gamma_{Y|X} = 1.57 \pm 0.48$ and $\sigma_{Y|X} = 0.14 \pm 0.02$. The above scaling

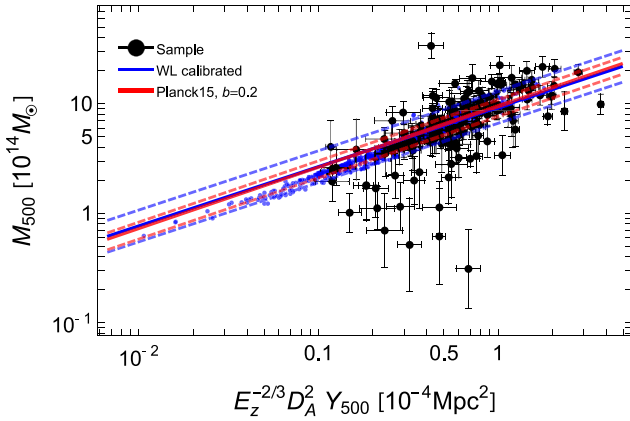


Figure 3. SZ flux versus mass. The black points with error bars picture the calibration sample, M_{WL} . The blue points picture the clusters with predicted masses M_{WLc} at the position of the measured SZ flux. The dashed blue lines show the median scaling relation (full blue line) plus or minus the intrinsic scatter at $z = 0.24$. The full red line shows the *Planck* derived relation, assuming a bias $b_{\text{SZ}} = -0.2$. The dashed red lines show the *Planck* relation for null bias (lower bound) and for $b_{\text{SZ}} = -0.4$ (upper bound).

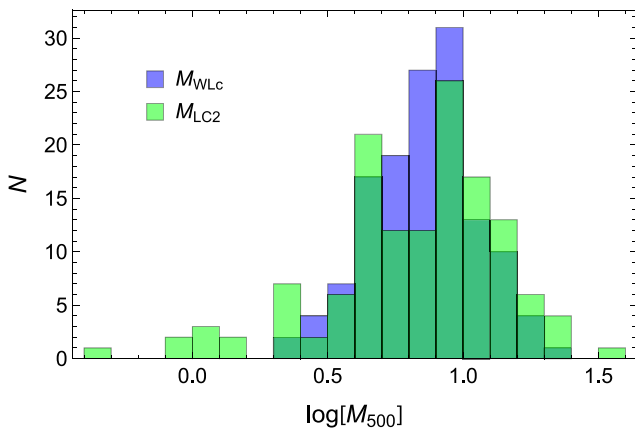


Figure 4. Histograms of the logarithm of the WL calibrated mass (M_{WLc} , blue charts) and of the original masses M_{LC2} (green charts) for the calibration sample in the analysis of the *Planck* clusters. Masses are in units of $10^{14} M_{\odot}$.

could be used to predict masses only with the caveats discussed in Section 3.

We stress that equation (32) is functional to mass estimates. It cannot be compared to self-similar models or results from numerical simulations since it does not deal with the intrinsic scatter in the SZ flux (CoMaLit-II). We do not need to model this scatter if we are only interested in mass prediction.

For a detailed discussion of the Y_{500} – M_{500} scaling we refer to CoMaLit-II and CoMaLit-IV.

Due to the regularization process and the bias correction, the distribution of WL calibrated masses is more regular than that of the original WL masses from the calibration sample (see Fig. 4). Measurements at either the very high or the very low end of the mass spectrum are viewed as unlikely and the tails of the M_{WLc} distribution are less pronounced.

The distribution of *Planck* selected clusters with known counterparts with redshift in the mass–redshift (M_{500} – z) plane, using the WL calibrated proxy, is shown in Fig. 5. Apart from the shift

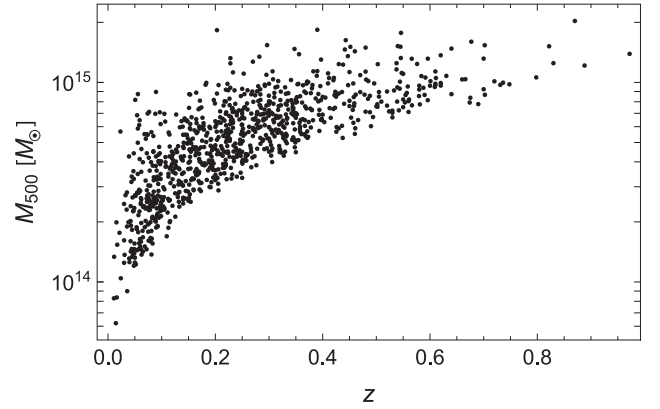


Figure 5. Distribution of the 926 PSZ2-MMF3 clusters with known redshift in the M_{500} – z plane. Masses are WL calibrated.

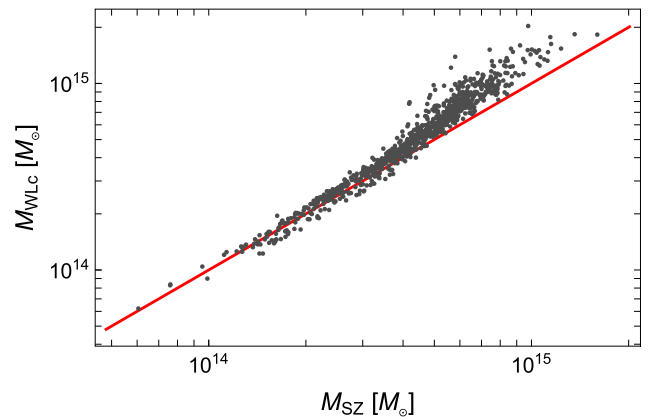


Figure 6. *Planck* SZ masses M_{SZ} versus WL calibrated masses M_{WLc} for the MMF3 clusters with measured redshift. Masses are in units of M_{\odot} . The red line shows the bisection $M_{\text{SZ}} = M_{\text{WLc}}$.

towards higher masses, the distribution agrees with the results in *Planck* Collaboration XXVII (2016a).

6.4 WL versus SZ calibration

The computed WL calibrated masses differ substantially from the SZ masses (see Figs 6 and 7). We can look for mass or redshift dependences of the bias in the full sample.

Analogously to Section 6.2, the bias for the full *Planck* sample can be computed by comparison with the WL calibrated masses, M_{WLc} . The full sample includes *Planck* clusters either with or without WL counterparts. We found $b_{\text{SZ}} = -0.17 \pm 0.01$, in line with the bias computed for the subsample of *Planck* clusters in the LC²-single by comparison with the direct M_{WL} measurements (see Table 3).

The *Planck* clusters with WL counterparts only probe the high-mass tail of the sample. The agreement between the two estimates suggests that the bias is not mass dependent. This conclusion seems to be at odds with Fig. 6, where the discrepancy between WL and SZ calibrated masses is more pronounced for massive clusters. However, this feature is driven by the high-mass clusters preferentially selected at high redshift. We then considered both the mass and the redshift dependence,

$$\ln(M_{\text{SZ}}) = b_{\text{SZ}} + \beta_{\text{SZ}} \ln(M_{\text{WLc}}) + \gamma_{\text{SZ}} T, \quad (33)$$

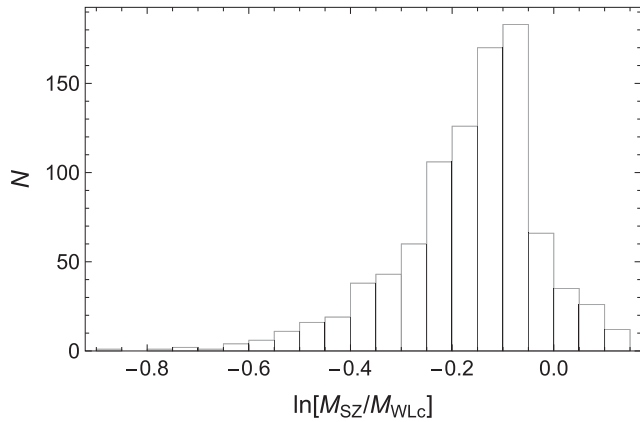


Figure 7. Histogram of the logarithm of the ratio of the *Planck* SZ masses M_{SZ} to the WL calibrated masses M_{WLC} for the MMF3 clusters with measured redshift.

where $T = \log F_z$. We found $b_{SZ} = 0.05 \pm 0.11$, $\beta_{SZ} = 0.94 \pm 0.08$ and $\gamma_{SZ} = -2.40 \pm 0.63$. This confirms that the bias is nearly mass independent, but it is significantly more pronounced at high redshifts.

7 THE SDSS REDMAPPER CATALOGUE

Optical richness or luminosity of galaxy clusters as measured from large surveys is often used as a mass proxy. Wen & Han (2015) collected and corrected cluster mass measurements based on X-ray or SZ observations and calibrated the rescaled total r -band luminosity to derive the mass of the clusters in the WHL (Wen, Han & Liu 2012) catalogue.

Here, we consider the Sloan Digital Sky Survey (SDSS) redMaPPer (red-sequence Matched-filter Probabilistic Percolation) catalogue, which was compiled by applying a red-sequence cluster finder to the DR8 release of the SDSS, covering $\sim 10\,000 \text{ deg}^2$ (Rykoff et al. 2014). The resulting catalogue⁷ contains $\sim 26\,000$ candidate clusters over the redshift range $0.08 \lesssim z \lesssim 0.55$. When available, we considered the spectroscopic redshift. Otherwise, we used the photometric redshift.

The WL mass is available for 149 redMaPPer clusters. We identified counterparts in the LC²-single catalogue by matching pairs whose redshifts differ by less than $\Delta z = 0.05$ and whose angular separation in the sky does not exceed 5 arcmin.

7.1 The proxy

The redMaPPer optical richness λ of a cluster is defined as the sum of the probabilities of the galaxies found near a cluster to be actually cluster members. All galaxies above a cut-off luminosity and below a distance radial cut which scales with richness are considered. According to our notation, the proxy is $x = \log \lambda$.

7.2 Selection effects

Clusters are included in the catalogue if λ exceeds 20 times the scalefactor S_{RM} , which is a function of the photometric redshift of the cluster. This criterion approximately selects clusters with at

least 20 galaxy counts above the flux limit of the survey or the cut-off luminosity at the cluster redshift, whichever is higher (Rykoff et al. 2014). We denote the threshold for the i -th proxy as

$$x_{th,i} = \log(20S_{RM,i}). \quad (34)$$

The effect of the selection threshold is twofold. First, it skews the conditional probability of the observed value, x , given the true value, X (see Section 3.3.2). This is modelled as

$$p(x|X) \propto \mathcal{N}(X, \delta_x^2) \mathcal{U}(x - x_{th}). \quad (35)$$

Secondly, since the threshold is approximately constant (for most of the clusters $S_{RM,i} \sim 1$), the intrinsic distribution of richnesses is skewed too. We model the distribution of the proxies as a smoothly truncated Gaussian,

$$P(X) \propto \mathcal{N}(\mu_X, \sigma_X^2) \text{erfc}\left(\frac{\mu_X - X}{\sqrt{2}\sigma_X}\right), \quad (36)$$

where the low value tail of the normal distribution \mathcal{N} is suppressed by the complementary error function.⁸ In our regression analysis, we treated the effective threshold μ_X as known and time independent. We fixed it at the minimum of the measured $x_{th,i}$.

Alternatively, we also considered a threshold that is constant and equal to the minimum of the measured $x_{th,i}$ up to $z \sim 0.4$ and then steeply increases with z to mimic the time dependence of the lower envelope of the observed richnesses.⁹ We checked that variations in final results are negligible and that this parametrization does not improve the modelling of the distribution of richness as a function of redshift. In the following, we will discuss the reference case only.

The transition length σ_X was left as a free, time-independent parameter of the regression.

Mean μ_X and standard deviation σ_X of the normal distribution can evolve with redshift as formalized in CoMaLit-IV.

7.3 The masses

We considered WL masses within r_{200} , which better matches the region analysed by the redMaPPer algorithm. The catalogue of WL calibrated masses is released with the paper. An extract is presented in Table 5. The redMaPPer catalogue of WL calibrated masses spans one decade in mass from $M_{200} \sim 2 \times 10^{14} M_\odot$ to $\sim 2.5 \times 10^{15} M_\odot$. The typical mass is $M_{200} \sim 3.1 \times 10^{14} M_\odot$ with a dispersion of $\sigma_M \sim 10^{14} M_\odot$. It samples the high mass end of the halo mass function up to redshift $z = 0.55$.

The fitted conditional probability for the calibration sample is

$$Y \sim \mathcal{N}(Y_X = \alpha_{Y|X} + \beta_{Y|X} X + \gamma_{Y|X} T, \sigma_{Y|X}^2), \quad (37)$$

with $\alpha_{Y|X} = -0.92 \pm 0.17$, $\beta_{Y|X} = 0.94 \pm 0.09$, $\gamma_{Y|X} = -0.16 \pm 0.55$ and $\sigma_{Y|X} = 0.21 \pm 0.02$.

WL calibrated masses are shown in Fig. 8. Due to the cut-off in richness, most of the redMaPPer clusters are beyond the peak of the richness distribution. As discussed in Section 3.3.1, these measured λ are likely overestimated. In the plot of the predicted M_{WLC} versus the observed richness in Fig. 8, they lie on the right of the estimated scaling relation, which aligns the true values of mass and richness.

The distribution of redMaPPer selected clusters in the mass–redshift (M_{200} – z) plane, using the WL calibrated proxy, is shown in Fig. 9. The mass limit of the sample is nearly constant at $M_{200} \gtrsim 2.1 \times 10^{14} M_\odot$ up to $z \sim 0.4$ and then slowly increases

⁷ The latest version of the catalogue at the time of writing is v6.3. It is available at <http://risa.stanford.edu/redMaPPer/>

⁸ In the notation of Table 1, $\mu_X = \mu_{Z_{min}}$ and $\sigma_X = \sigma_{Z_{min}}$.

⁹ This feature is not available in the public release of the LIRA package.

Table 5. The first 10 entries of the catalogue of WL calibrated masses of the redMaPPer clusters, REDMAPPER_DR8_PUBLIC_V6.3_MWLC.DAT. The full catalogue is available in the electronic form. Column 1: index of detection. Column 2: name of redMaPPer detection. Columns 3, 4 and 5: right ascension, declination (J2000) and redshift. Columns 6 and 7: WL calibrated mass, M_{WLc} , and associated error. Columns 8 and 9: WL mass of the LC²-single counterpart, M_{LC2} , and associated error. Masses are within r_{200} and they are in units of $10^{14} M_{\odot}$.

Index	Name	RA	Dec.	z	M_{WLc}	$M_{\text{WLc_ERR}}$	M_{LC2}	$M_{\text{LC2_ERR}}$
1	RMJ155820.0+271400.3	239.580	27.233	0.0948	15.324	1.732	12.457	2.095
2	RMJ164019.8+464241.5	250.080	46.712	0.2328	17.670	1.829	16.951	2.677
3	RMJ131129.5–012028.0	197.870	−1.341	0.1824	14.793	1.428	18.857	1.286
5	RMJ090912.2+105824.9	137.300	10.974	0.1705	15.635	1.619	11.333	3.667
6	RMJ133520.1+410004.1	203.830	41.001	0.2317	16.801	1.692	23.729	3.943
7	RMJ003208.2+180625.3	8.034	18.107	0.3976	21.265	2.578	NA	NA
8	RMJ224319.8–093530.9	340.830	−9.592	0.4410	25.295	3.468	29.330	5.587
9	RMJ100214.1+203216.6	150.560	20.538	0.3237	13.457	1.115	NA	NA
11	RMJ082529.1+470800.9	126.370	47.134	0.1277	11.968	1.164	NA	NA
13	RMJ091753.4+514337.5	139.470	51.727	0.2269	13.785	1.226	14.257	1.986

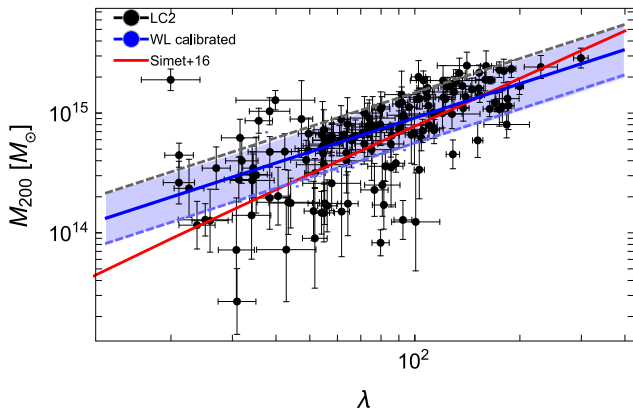


Figure 8. Optical richness λ versus mass. The black points with error bars picture the calibration sample, M_{LC2} . The blue points picture the clusters with predicted masses M_{WLc} at the position of the measured λ . The dashed blue lines show the median scaling relation (full blue line) plus or minus the intrinsic scatter at $z = 0.37$. The shaded blue region encloses the 68 per cent confidence region around the median relation due to uncertainties on the scaling parameters. The red line is the relation adapted from Simet et al. (2017b).

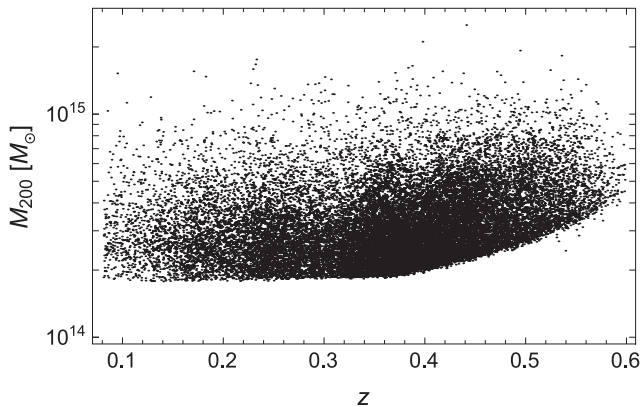


Figure 9. Distribution of the redMaPPer clusters in the M_{200} – z plane. Masses are WL calibrated.

up to the redshift limit of the sample. This flatness mirrors the selection properties of the redMaPPer catalogue, which is nearly complete at $z \lesssim 0.3$ for $\lambda \gtrsim 30$ (Rykoff et al. 2014).

7.4 Note added

Mass calibration of redMaPPer clusters has been very recently addressed by a couple of papers, one of them posted to the public archive just before (Farahi et al. 2016) and the other one just after (Simet et al. 2017b) the first submission of this paper.

Farahi et al. (2016) calibrated the mass of redMaPPer clusters with a stacked spectroscopic analysis of simulated galaxy surveys. They found $\beta_{Y|X} = 1.31 \pm 0.06_{\text{stat}} \pm 0.13_{\text{sys}}$ at redshift $z = 0.2$, slightly steeper than our result.

Simet et al. (2017b) performed a measurement of the mass–richness relation of the redMaPPer galaxy cluster catalogue using stacked WL data of 5570 cluster in the redshift range $0.1 \lesssim z \lesssim 0.33$ from the SDSS. They found a power-law index of 1.33 ± 0.09 .

This result is marginally consistent with ours (see Fig. 8). The relations nearly agree at the very massive end. However, our derived scaling relation (see equation 37) is shallower and it corresponds to more massive clusters at the low richness end.

The source of disagreement may be the different treatment of the Eddington bias, illustrated in Section 3.3.1, which is very significant for the redMaPPer clusters. In fact, the peak of the richness distribution is just beyond the threshold $\lambda \sim 20$. Due to error measurements most of the measured richnesses are then larger than the true richnesses. The measured richnesses are consistently on the right side with respect to the scaling (see Fig. 8). The bias is more significant at the smaller richnesses, where the relative errors are larger. To account for this, LIRA can model the richness distribution as a redshift-evolving normal probability density smoothly truncated at the low end.

This means that the different scaling relations cannot be compared straightaway. Our scaling relation refers to the true richness, whereas the scaling relation in Simet et al. (2017b) refers to the measured richness. The comparison to be fair, we should not compare the scaling relations but the forecasted masses. In a sense, the scaling in Simet et al. (2017b) can be suitable for forecasting, but it is not representative of the ‘true’ scaling relation. On the contrary, to use our scaling relation for forecasting we should plug in the unbiased richnesses (see Section 3).

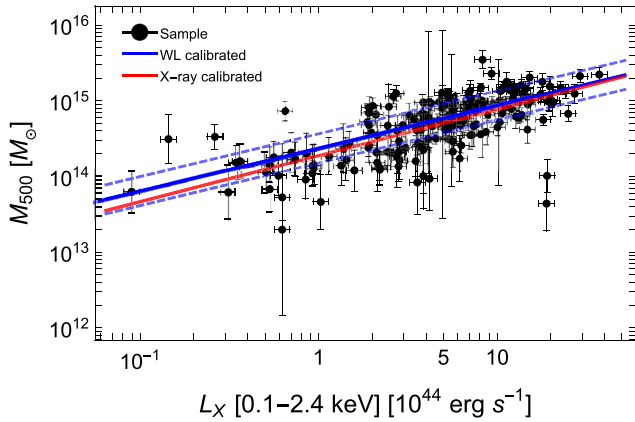


Figure 10. Soft band luminosity versus mass M_{500} . The black points with error bars picture the calibration sample, M_{LC2} . The blue points picture the clusters with predicted masses M_{WLC} at the position of the measured luminosity. The dashed blue lines show the median scaling relation (full blue line) plus or minus the intrinsic scatter. The red line tracks the scaling relation from Arnaud et al. (2010) used to calibrate X-ray masses in Piffaretti et al. (2011). Lines refer to the median redshift $z = 0.122$. Masses are in units of M_{\odot} .

8 MCXC

The MCXC (Meta-Catalogue of X-ray detected Clusters of galaxies; Piffaretti et al. 2011) comprises 1743 unique X-ray clusters collected from available *ROSAT* All Sky Survey-based and serendipitous cluster catalogues.

X-ray luminosities were systematically homogenized to the [0.1–2.4] keV band and standardized to an overdensity of $\Delta = 500$. Uncertainties are not provided. For our analysis, we fixed the statistical uncertainty on the luminosity to 10 per cent. As the LC^2 , the MCXC is not statistically complete.

Luminosities within r_{500} quoted in the MCXC catalogue were mostly obtained by rescaling the total luminosity under the assumption of a universal density profile or they were computed iteratively from the available aperture luminosities by assuming the L – M relation from Arnaud et al. (2010). The same L – M was also used to estimate M_{500} , which we refer to as M_X in the following.

MCXC and LC^2 -single share 196 clusters, which constitute our calibration subsample. We identified counterparts in the LC^2 -single catalogue by matching pairs whose redshifts differ for less than

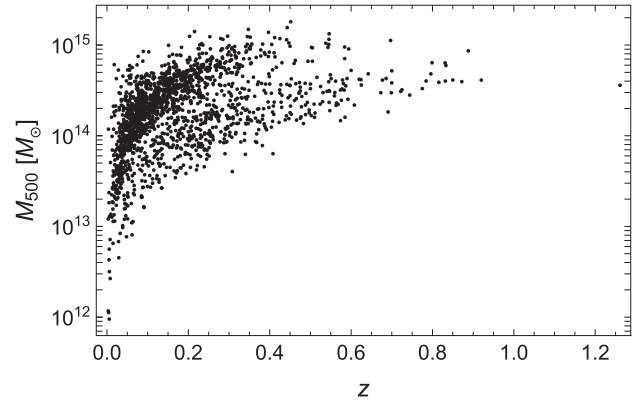


Figure 11. Distribution of the MCXC clusters in the M_{500} – z plane. Masses are WL calibrated and in units of M_{\odot} .

$\Delta z = 0.05$ and whose angular separation in the sky does not exceed 2 arcmin.

WL calibrated masses are shown in Fig. 10. The catalogue of WL calibrated masses is released with the paper. An extract is presented in Table 6. The MCXC clusters cover a large mass range. WL calibrated masses go from $M_{500} \sim 2 \times 10^{12} M_{\odot}$ to $\sim 2 \times 10^{15} M_{\odot}$, with a typical value of $M_{500} \sim 2.3 \times 10^{14} M_{\odot}$ and with a dispersion of $\sigma_M \sim 1.9 \times 10^{14} M_{\odot}$. The catalogue spans a large redshift interval from the local universe to $z \lesssim 1.3$, with a median redshift of $z = 0.136$.

Due to the heterogeneous nature of the MCXC catalogue, we could not correct for any distant-dependent Malmquist bias. The composite selection criteria made the proxy distribution smooth without truncation at the lower end. We modelled it as a simple redshift-evolving Gaussian distribution. In this simple framework, the WL calibrated masses and the measured luminosities align very well with the scaling relation (see Fig. 10). Since we could not fully correct for selection effects, some biases can persist (see Section 9).

The distribution of MCXC clusters in the mass–redshift (M_{500} – z) plane, using the WL calibrated mass proxy, is shown in Fig. 11. Notwithstanding the heterogeneous selection criteria used to compile the sample, the mass limit steadily increases with redshift. However, we can distinguish two populations with quite distinct mass limits. MCXC exploits both RASS-based and serendipitous surveys. At a given redshift, serendipitously discovered clusters are less luminous and massive than those from RASS-based catalogues

Table 6. The first 10 entries of the catalogue of WL calibrated masses of the MCXC clusters, MCXC_MWLC.DAT. The full catalogue is available in electronic form. Column 1: index of detection. Column 2: name of the detection. Columns 3 and 4: right ascension and declination (J2000) of the MCXC cluster. Column 5: redshift of the cluster; Columns 6 and 7: WL calibrated mass M_{WLC} and associated error. Columns 8 and 9: WL mass of the LC^2 -single counterpart, M_{LC2} , and associated error. Column 10: X-ray mass proxy M_X from the MCXC catalogue. Masses are within r_{500} and they are in units of $10^{14} M_{\odot}$.

Index	Name	RA	Dec	z	MWLC	MWLC_ERR	MLC2	MLC2_ERR	MX	MX_ERR
1	MCXC_J0000.1+0816	0.030	8.274	0.0396	0.757	0.130	NA	NA	0.737	NA
2	MCXC_J0000.4–0237	0.103	–2.625	0.0379	0.342	0.077	NA	NA	0.330	NA
3	MCXC_J0001.6–1540	0.412	–15.681	0.1246	1.792	0.211	NA	NA	1.656	NA
4	MCXC_J0001.9+1204	0.488	12.073	0.2033	3.073	0.277	NA	NA	2.693	NA
5	MCXC_J0003.1–0605	0.799	–6.086	0.2320	6.062	0.471	5.886	1.214	5.219	NA
6	MCXC_J0003.2–3555	0.801	–35.927	0.0490	1.236	0.175	NA	NA	1.202	NA
7	MCXC_J0003.8+0203	0.961	2.063	0.0924	1.834	0.217	NA	NA	1.734	NA
8	MCXC_J0004.9+1142	1.247	11.701	0.0761	1.364	0.184	NA	NA	1.301	NA
9	MCXC_J0005.3+1612	1.344	16.211	0.1164	2.674	0.270	NA	NA	2.493	NA
10	MCXC_J0006.0–3443	1.513	–34.724	0.1147	2.904	0.284	NA	NA	2.712	NA

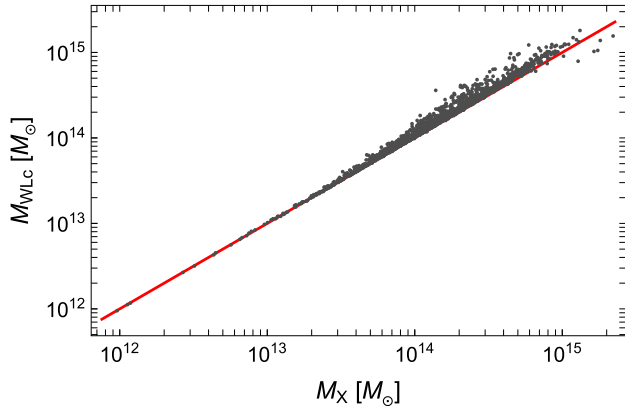


Figure 12. MCXC masses, M_X , versus WL calibrated masses, M_{WLC} . Masses are in units of M_\odot . The red line shows the bisection $M_X = M_{WLC}$.

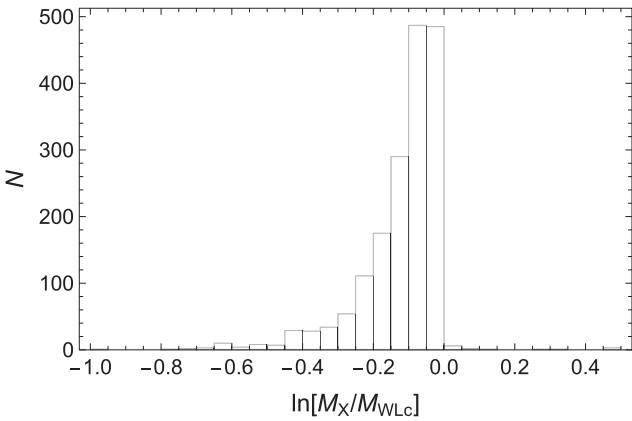


Figure 13. Histogram of the logarithm of the ratio of the MCXC masses M_X to the WL calibrated masses M_{WLC} .

because the deeper exposures allow lower flux limits to be adopted (Piffaretti et al. 2011).

8.1 WL versus X-ray calibration

The WL calibrated masses differ from the X-ray masses that are underestimated on average by ~ 14 per cent (see Figs 12 and 13). In fact, our estimated scaling relation has a higher normalization than that used in Piffaretti et al. (2011, see Fig. 10). Most of the off-set can be attributed to the hydrostatic bias. Hydrostatic masses or X-ray calibrated masses can be underestimated by 20–30 per cent due to non-thermal sources of pressure in the gas, to unvirialized bulk motions and subsonic turbulence, to temperature inhomogeneity, and, to a lesser degree and mainly in the external regions, to the presence of clumps (Battaglia et al. 2012; Rasia et al. 2012; Sereno & Ettori 2015b).

We can look for mass or redshift dependences of the bias. We proceeded as in Section 6.4 by comparing the WL to the X-ray calibrated masses of all the MCXC clusters. We fitted the relation

$$\ln(M_X) = b_X + \beta_X \ln(M_{WLC}) + \gamma_X T. \quad (38)$$

The X-ray calibrated masses in the MCXC catalogue are provided without uncertainties. We adopted a statistical uncertainty of ~ 40 per cent, which reflects the intrinsic scatter of the X-ray luminosities in the MCXC catalogue (CoMaLit-IV).

Table 7. Comparison of the WL calibrated masses within r_{500} of the PSZ2, redMaPPer and MCXC catalogues. We quote the mean \ln differences in mass for sample pairs. Entries are in the format: $(N_{cl}), \mu(\pm\delta\mu) \pm \sigma(\pm\delta\sigma)$, where N_{cl} is the number of clusters in common between the samples; μ is the central estimate of the difference in natural logarithm $\ln(M_{500}^{row}/M_{500}^{col})$, with associated uncertainty $\delta\mu$; σ is the dispersion with associated uncertainty $\delta\sigma$. M_{500}^{row} (M_{500}^{col}) refers to the sample indicated in the corresponding row (column). Quoted values are the bi-weight estimators.

	PLANCK	MCXC
		(370)
PLANCK	–	$0.17(\pm 0.01)$ $\pm 0.23(\pm 0.01)$
	(189)	(324)
redMaPPer	$-0.03(\pm 0.02)$ $\pm 0.30(\pm 0.02)$	$0.24(\pm 0.03)$ $\pm 0.46(\pm 0.02)$

The bias is nearly mass independent ($\beta_X = 1.02 \pm 0.01$). In the local universe ($z = 0.01$), the bias is negligible ($b_X = -0.02 \pm 0.01$), but it becomes more prominent with redshift ($\gamma_X = -3.2 \pm 0.2$).

This is the same trend found for SZ calibrated masses (see Section 6.4). In fact, we are using the same calibration sample, LC²-single. Any trend in the mass calibration can be only ascribed to redshift dependences.

Simet et al. (2017a) used stacked WL measurements to calibrate the average masses for 166 luminous MCXC clusters. They found evidence that the M_X s are approximately 15–30 per cent lower than the WL masses over the range of masses probed in their subsample ($0.9\text{--}15 \times 10^{14} M_\odot$), in agreement with our result.

9 CATALOGUE COMPARISON

The PSZ2, the redMaPPer and the MCXC samples have a certain degree of superposition, which allowed us to check for consistency in our WL calibrated masses. Results are summarized in Table 7 and Figs 14 and 15.

We identified clusters in catalogue pairs by matching clusters whose redshifts differ for less than $\Delta z = 0.05$ and whose angular separation in the sky does not exceed 2 arcmin.

WL calibrated masses for the redMaPPer clusters are within r_{200} . To compare with *Planck* and MCXC clusters, whose masses are within r_{500} , we rescaled the redMaPPer masses assuming a Navarro–Frenk–White profile (Hu & Kravtsov 2003; Sereno 2015) with the mass–concentration relation derived in Bhattacharya et al. (2013), which we rescaled to the value of σ_8 , i.e. the amplitude of the matter power spectrum, found by the latest *Planck* cosmological analysis (Planck Collaboration XIII 2016b). We checked that the dependence of the rescaling on the adopted mass–concentration relation and cosmological parameters is negligible by also considering alternative derivations (see e.g. Dutton & Macciò 2014).

The WL calibrated masses show good agreement (see Table 7). Discrepancies are statistical and well within the dispersion values. This is comfortable since we used the same calibration catalogue of WL masses, i.e. LC²-single.

The WL calibrated masses and the SZ masses of the *Planck* clusters, whose comparison is depicted in Figs 6 and 7, relied on the same proxy measurements and were then correlated. The same consideration holds for the WL or X-ray calibrated masses of the MCXC clusters (see Figs 12 and 13). This correlation strongly

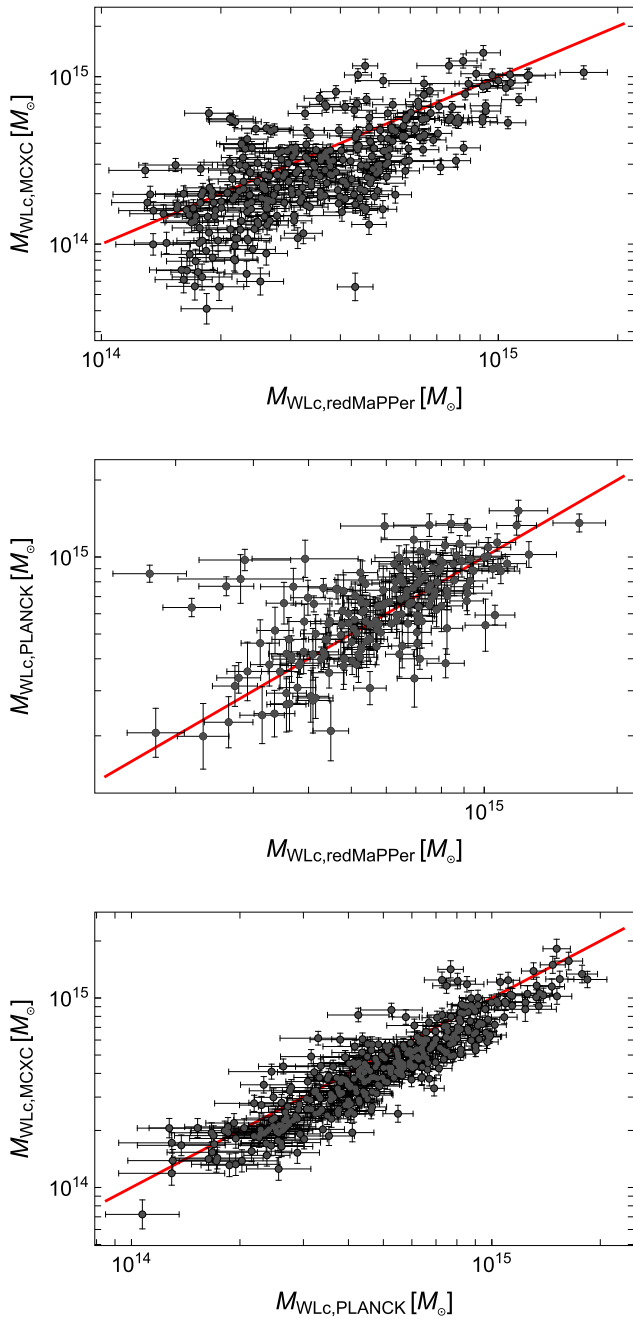


Figure 14. Top panel: WL calibrated mass of the redMaPPer clusters versus the masses of the MCXC clusters. Middle panel: WL calibrated masses of the redMaPPer clusters versus the masses of the *Planck* clusters. Bottom panel: WL calibrated masses of the PSZ2 clusters versus the masses of the MCXC clusters. The red lines show the bisectors. Masses are within r_{500} and they are in units of M_{\odot} .

reduces the scatter. On the other hand, WL calibrated masses of PSZ2, redMaPPer and MCXC clusters rely on independent proxies. This explains the quite large scatter in the mass comparison that mostly comes from the combined intrinsic scatters of the scaling relations. However, a good degree of correlation still persists, since the three catalogues of WLc masses exploited the same calibration catalogue, i.e. LC²-single. This prevented us from combining the WLc masses a posteriori.

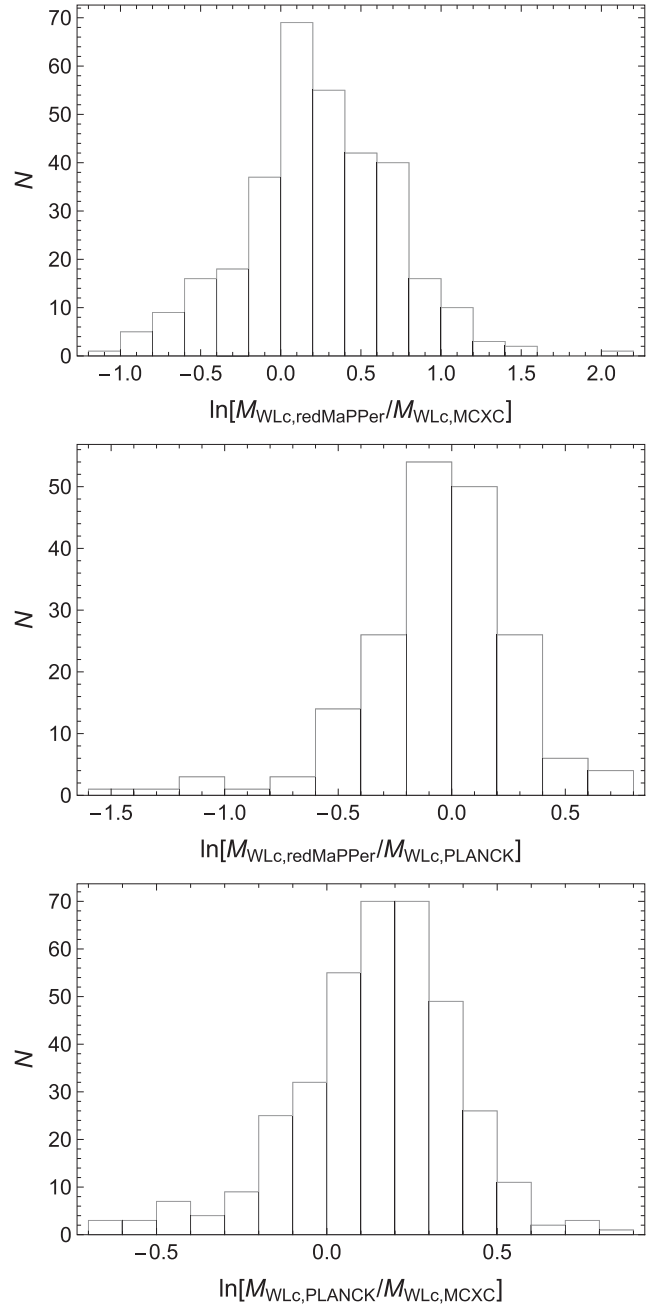


Figure 15. Top panel: histogram of the natural logarithm of the ratio of the WLc masses of the redMaPPer clusters to the WLc masses of the MCXC clusters. Middle panel: histogram of the natural logarithm of the ratio of the WLc masses of the redMaPPer clusters to the WLc masses of the PSZ2 clusters. Bottom panel: histogram of the natural logarithm of the ratio of the WLc masses of the PSZ2 clusters to the WLc masses of the MCXC clusters.

Whereas forecasted masses are in agreement and differences are smaller than the statistical scatter, we found a tentative trend for the WL calibrated masses of the MCXC clusters to be overestimated in comparison to either the redMaPPer or the PSZ2-based estimates. This can be ascribed to some residual selection effect. Most clusters in the MCXC sample were flux-selected, but we could not correct for the Malmquist bias due to the unknown observational thresholds, which are not provided in the catalogue. The X-ray luminosities of the clusters near the threshold are likely overestimated, which in turn overestimate the mass predictions.

Table 8. Comparison of WL masses within r_{500} from independent analyses. Entries are as in Table 7.

	CLASH (6)	LoCuSS (21)	WtG (17)
CCCP	$-0.58(\pm 0.22)$ $\pm 0.28(\pm 0.20)$	$0.02(\pm 0.09)$ $\pm 0.39(\pm 0.09)$	$-0.22(\pm 0.07)$ $\pm 0.25(\pm 0.06)$
CLASH	–	$0.13(\pm 0.09)$ $\pm 0.13(\pm 0.10)$	$0.07(\pm 0.13)$ $\pm 0.40(\pm 0.07)$
LoCuSS	–	–	$-0.16(\pm 0.12)$ $\pm 0.37(\pm 0.07)$

Table 9. Comparison of WL masses within 1 Mpc from independent analyses. The notation follows Table 8.

	CLASH (6)	LoCuSS (21)	WtG (17)
CCCP	$-0.42(\pm 0.02)$ $\pm 0.03(\pm 0.03)$	$0.02(\pm 0.04)$ $\pm 0.22(\pm 0.07)$	$-0.15(\pm 0.04)$ $\pm 0.16(\pm 0.04)$
CLASH	–	$0.12(\pm 0.05)$ $\pm 0.09(\pm 0.08)$	$0.03(\pm 0.08)$ $\pm 0.26(\pm 0.05)$
LoCuSS	–	–	$-0.11(\pm 0.08)$ $\pm 0.25(\pm 0.05)$

10 RELIABILITY OF THE CALIBRATION SAMPLE

At the present time, there are three main reasons to prefer composite, heterogeneous WL compilations to homogeneous calibration catalogues. First, the significantly improved statistics. The largest available WL samples with homogeneous data-analysis and well-measured masses consist of nearly 50 clusters (see Table 2), an order of magnitude smaller than LC²-single.

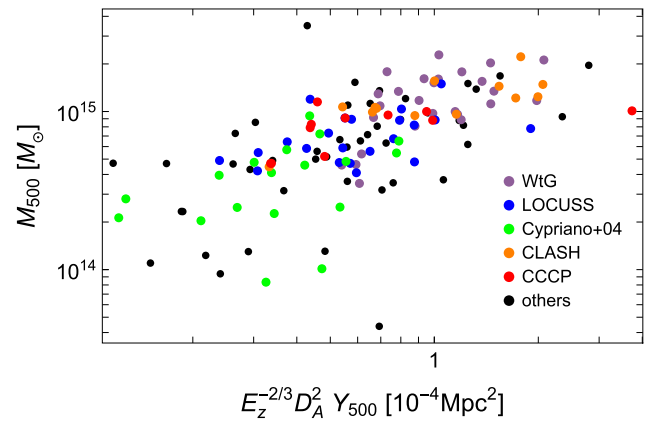
Secondly, current WL mass determinations by competing groups are not consistent (CoMaLit-I). Quoted statistical uncertainties of ~ 10 –20 per cent are smaller than the differences between independent mass determinations, which can be as large as ~ 50 per cent (see Tables 8 and 9). This discrepancy hints at systematic effects still to be fully understood. In the presence of slightly compatible or discrepant analyses, it can be safer to consider all the results rather than to arbitrarily prefer a single data set (Gott et al. 2001).

Thirdly, for clusters with multiple analyses LC²-single promotes the WL study exploiting the deepest observations and the most complete multiband coverage. Analyses based on the better data are hopefully the more reliable and systematics free. Further considerations on heterogeneous samples can be found in Piffaretti et al. (2011) and CoMaLit-III.

Ideally, one could introduce parameters that quantify the systematic off-sets of each subcatalogue relative to systematics-free measurements and associate priors to them. The systematic off-sets could then be solved simultaneously with the scaling relation. We do not pursue this full Bayesian treatment but in the following we check for systematics related to heterogeneity and the unknown selection function.

Table 10. Homogeneous subsamples in the WL calibration sample used for the *Planck* clusters. We list the subsamples in LC²-single with at least six *Planck* matches. Column 1: sample name. Column 2: number of clusters, N_{Cl} , in LC²-single with a *Planck* counterpart. Columns 3 and 4: typical redshift and dispersion. Columns 5 and 6: typical mass and dispersion. Typical values and dispersions are computed as bi-weighted estimators. Masses are in units of $10^{14} M_{\odot}$.

Sample	N_{Cl}	z	σ_z	M_{500}	$\sigma_{M_{500}}$
WtG	26	0.34	0.12	12.1	5.3
LoCuSS	22	0.22	0.04	6.8	2.5
Cypriano et al. (2004)	18	0.11	0.04	3.9	2.2
CLASH	13	0.37	0.13	11.3	3.3
CCCP	11	0.22	0.06	8.6	2.4
Gruen et al. (2014)	7	0.29	0.12	4.2	2.1
Oguri et al. (2012)	6	0.47	0.10	6.3	3.2

**Figure 16.** The composition of the LC²-single sample with PSZ2 counterparts. Masses of homogeneous subsamples with at least 10 matches with the *Planck* catalogue are plotted versus the SZ flux.

10.1 Heterogeneity

The above considerations are strong but general. They might fail in specific contexts. To further assess advantages, problematics and systematics related to heterogeneous calibration samples we focus in the following on the *Planck* clusters. The same kind of considerations hold for the redMaPPer and MCXC clusters, whose calibration WL samples have similar size and composition.

As shown in CoMaLit-II, the effect of the mass calibration is dramatic when considering the bias of *Planck* masses. The preference for a calibration sample drives the estimate of the bias. We repeated the analysis of Section 6.2 for some homogeneous samples. Results are summarized in Table 3. Estimated biases range from $b_{\text{SZ}} \sim -0.2$ to -0.4 . This is reflective of the inconsistent WL mass calibrations, which pushed us to consider LC²-single as the reference sample to minimize systematics. We remark that different samples probe different mass and redshift ranges. The measured bias has to be intended as a sample-weighted mean. However, mass and redshift differences in the various samples are not so large to explain the bias discrepancy, which is linked to inconsistent mass measurements.

The subsample of LC²-single with *Planck* counterparts used for calibration relies on 29 independent WL analyses, with only seven subsamples being represented by more than six clusters (see Table 10). There is substantial overlap among the different subsamples in both mass and redshift ranges (see Table 10 and Fig. 16).

This guarantees that any systematic error affecting single subsamples is compensated for, even though at the expense of an increased scatter.

To further assess the stability of the heterogeneous LC^2 -single as a calibration sample, let us consider a rather extreme pathological case, when the most represented subsample, i.e. the WtG subsample, has mass estimates systematically over- or underestimated. The WtG clusters sample the high-mass end of the cluster distribution and are expected to have significant leverage in the determination of the scaling relation. Notwithstanding these extreme circumstances, even the effect of a very significant systematic bias of ± 10 per cent would impact only a fraction of the full sample (the WtG subsample constitutes ~ 20 per cent of the total calibration sample) and we expect an overall systematic mass shift in the calibration sample of the order of $\sim \pm 2$ per cent.

We repeated the analysis of Section 6.3 assuming a systematic error in the WtG subsamples. A $+(-)10$ per cent systematic error produces an over- (under-) estimation of the WL calibrated masses of ~ 1.7 , 0.3 and 0.5 per cent for the clusters in the LC^2 catalogue, for the cluster with no WL counterpart and for the full *Planck* sample, respectively. As expected, even a large systematic effect is compensated by the composite nature of the calibration sample. It shows up mainly for clusters in the calibration samples, whereas its effect is very negligible for the clusters with no WL data.

The effect of a systematic error is further reduced by the Bayesian analysis. The WL calibrated masses are seen as unknown variables in the regression. Our employed Bayesian approach assumes that true masses are well behaved and align well along the scaling relation. Significant deviations off the scaling by some clusters, which characterize clusters affected by strong systematics, are penalized in the hierarchical model.

10.2 Unknown selection function

Most sources of scatter affect primarily one specific observable. However, some of them can affect several simultaneously (Stanek et al. 2010; Angulo et al. 2012). Common sensitivities to the internal structure, orientation and environment of clusters, as well as to line-of-sight superposition of uncorrelated structure, can make scatters between different mass-observable relations positively correlated (Angulo et al. 2012). The degree of this correlation is still to be firmly established. Results from numerical simulations strongly depend on adopted schemes and specific physical treatments.

Scatter covariance might affect our results since the selection function of the calibration sample is unknown. Let us make the hypothetical case that the calibration sample preferentially includes bright X-ray clusters. As a result of covariance among WL mass, SZ flux and X-ray luminosity, at fixed Y_{SZ} the calibration sample will preferentially include more massive (and less scattered) clusters than the entire *Planck* population. This will bias the measured scaling relation between mass and Compton parameter and the forecasted masses of the remaining population. Similar considerations might apply to richness and redMaPPer clusters.

Some arguments can be formulated to demonstrate that these biases should be negligible in our analysis. First, the LC^2 is an unfiltered collection of all the clusters and groups with measured WL mass (CoMaLit-III). The included clusters were originally detected within X-ray, optical, SZ or shear surveys. Serendipitous detections, follow-ups and targeted observations are included too. The WL signal is low and LC^2 mostly samples the very massive end of the halo mass function. Large and heterogeneous samples may reduce the effect of selection biases (CoMaLit-III). As far as mass and redshift

are considered, the LC^2 sample is an unbiased sub-sample of the *Planck* clusters with very high signal-to-noise ratio (CoMaLit-II). The price to pay for heterogeneity is the increased scatter.

Secondly, the unbiased nature of our calibration subsamples is further indicated by the analysis of the completeness. In the CoMaLit approach, the completeness function can be estimated from the data together with the scaling relation (CoMaLit-IV). In fact, the completeness functions of the *Planck* and redMaPPer clusters in LC^2 -single follow those of the parent populations (see the upper panels in Figs 6 and 8 and related discussion in CoMaLit-IV).

Finally, for a more quantitative assessment of the bias related to the selection function of the calibration subsample, we tested our forecasting procedure on a toy-population of clusters. We simulated the pathologic case of X-ray luminous clusters preferentially included in the calibration subsample. In the following, we consider the case of the $M_{WL}-Y_{SZ}$ relation but similar results apply to the richness.

Here, we use arbitrary units such that the cluster with unitary mass has unitary SZ flux and X-ray luminosity too. We simulated a lognormal parent population of masses with $\langle \log M \rangle = 0$ and $\sigma_{\log M} = 0.5$. All simulated haloes lie at the same redshift. The observables are self-similarly related to the true mass,

$$M_{WL} = M, \quad (39)$$

$$Y_{SZ} = M^{5/3}, \quad (40)$$

$$L_X = M^{4/3}. \quad (41)$$

In the above equations, we neglected the redshift-dependence since the redshift is constant. For the aims of this testing, we do not have to specify the overdensity radius.

Observed values of WL mass, Compton integrated parameter and X-ray luminosity were simulated by scattering the self-similar values. We considered intrinsic scatters of $\sigma_{\log M_{WL} | \log M} = 0.1$, $\sigma_{\log Y_{SZ} | \log M} = 0.1$ and $\sigma_{\log L_X | \log M} = 0.15$ in line with results from CoMaLit-IV. Scatter values are strictly related to the measurement methodology and to the sample properties. Here, we just need approximated values. Conditional scatters were correlated through the factors $\rho_{\log M_{WL} \log Y_{SZ}} = 0.6$, $\rho_{\log M_{WL} \log L_X} = 0.4$ and $\rho_{\log Y_{SZ} \log L_X} = 0.5$ in line with the results of Angulo et al. (2012) based on the Millennium-XXL simulation. We were interested in systematic effects and neglected measurement uncertainties.

To test our regression method, we selected clusters in X-ray luminosity and then we estimated the $M_{WL}-Y_{SZ}$ relation without using the information on the selection and on the scatter correlation. A calibration sample of 100 objects was randomly drawn from the parent population of clusters with $\log L_X > \sigma_{\log L_X} = (4/3)\sigma_{\log M}$. In analogy to our real cases, we limited the calibration sample to the bright end.

As a first check, we recovered the self-similar relation, $M = Y_{SZ}^{3/5}$, by regressing the SZ fluxes versus the WL masses of the only clusters in the calibration sample. In the regression, we considered conditional scatters with respect to the true mass for both M_{WL} and Y_{SZ} , but we neglected the scatter correlation. We used a smoothly truncated Gaussian distribution to model the distribution of the unscattered values of the SZ fluxes. We did not model the Malmquist bias related to the selection in X-ray luminosity.

This simplified regression scheme is accurate enough to recover the true scaling relation. In Fig. 17, we show the deviations of the normalizations and the slopes from the true values for 1000 simulated samples.

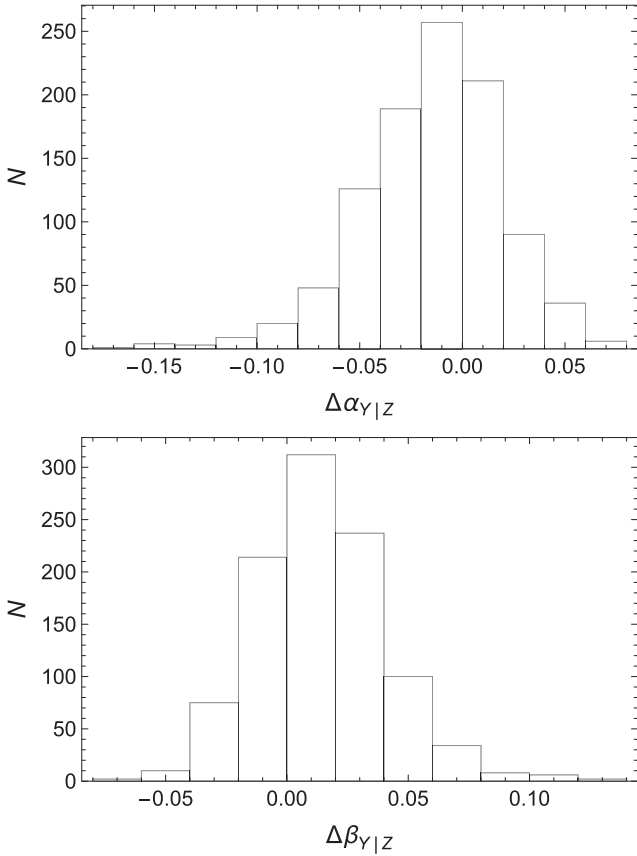


Figure 17. Top panel: histogram of the differences between the measured normalizations and the true one for the $M_{\text{WL}} - Y_{\text{SZ}}$ simulated samples selected in X-ray luminosity. Bottom panel: same as above but for the slope.

Most of the selection effects are accounted for with a proper modelling of the covariate distribution. Since the sample size of 100 objects is quite small, we cannot constrain the scatter correlation from the data. However, the wrongly assumed values of $\rho_{\log M_{\text{WL}}, \log Y_{\text{SZ}}} = 0.0$ has a negligible effect. Notwithstanding the systematic errors in the modelling, the self-similar relation of the full population was well recovered.

As a second check, we considered the effect of scatter covariance in forecasting. The calibration sample was selected as before, whereas the 530 masses to be forecasted were drawn from the population of low-luminosity clusters, i.e. $\log L_X < (4/3)\sigma_{\log M}$. We neglected the conditional scatter in the covariate variable and modelled the covariate distribution, including both the calibration subsample and the clusters with unknown masses, as a Gaussian. We simulated 10 samples to estimate the systematic errors in mass forecasting associated with the unknown selection function of the calibration sample and to the unknown (and not modelled) scatter covariance. Differences between true and recovered masses are shown in Fig. 18. As for the scaling relation, masses are well recovered.

To the present level of accuracy, the systematic biases discussed in this section are small with respect to the statistical uncertainties and can be neglected. The main limitation brought by the heterogeneous calibration sample is the increased conditional scatter of the WL masses with respect to the true masses and the related loss of accuracy in mass forecasting.

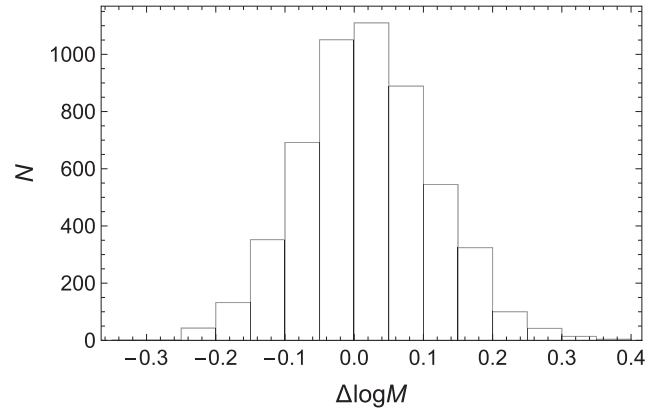


Figure 18. Histogram of the differences between the measured masses and the true one for the $M_{\text{WL}} - Y_{\text{SZ}}$ simulated samples selected in X-ray luminosity.

11 CONCLUSIONS

Mass prediction given a proxy can be efficiently performed in the context of Bayesian hierarchical modelling. The key to efficiency is a proper treatment of measurement errors, Malmquist/Eddington biases, selection effects and redshift evolution.

Our proposed statistical method performs mass forecasting together with the determination of the scaling relation. Mass calibration relies on a reference subsample of clusters with measured masses. This subsample does not have to be representative of the full sample, whose distribution is modelled in the regression. However, we still assume that the scaling relation and the conditional scatter of the subsample can characterize the full sample. Thanks to the simultaneous determination of masses, scaling relation and proxy distribution, systematics are strongly reduced and statistical errors are properly assessed.

We applied the CoMaLit mass forecasting to three widely used cluster samples: the PSZ2 catalogue of *Planck* detected clusters, the redMaPPer catalogue of red-sequence filtered clusters and the meta-catalogue of X-ray detected clusters MCXC. As calibration sample, we considered the subsamples of clusters with measured WL mass. Catalogues of WL calibrated masses are released with the paper. The Bayesian analysis was performed with the publicly available R-package LIRA.

The considered samples were not selected by their WL properties. The PSZ2 and the redMaPPer catalogues were selected by SZ flux and optical richness, respectively. The MCXC clusters were selected based on their X-ray properties. We considered the full catalogues and treated the masses of clusters without WL estimates as missing data. As far as the calibration subsample with measured WL masses follows the scaling relation of the full sample and it is affected by the same intrinsic scatter, there are no major selection effects related to the WL measurements. Accordingly, we modelled the distribution of the full sample, not the distribution of the subsample with measured WL mass.

Planck's cluster count cosmology results (Planck Collaboration XXIV 2016c) favour smaller values of the amplitude of the matter power spectrum, σ_8 , and of the matter density parameter, Ω_M , than those from the *Planck*'s measurements of the primary CMB temperature anisotropies (Planck Collaboration XIII 2016b). The mass bias required to reconcile the two experiments is larger than current results and corresponds to $b_{\text{SZ}} = -0.42 \pm 0.04$ (Planck Collaboration XXIV 2016c). This assumes that the mass bias does not depend on cluster mass and redshift.

We found that whereas the average bias is $b_{SZ} \sim -0.25$, which it is not enough to explain the disagreement, it is strongly redshift dependent. SZ masses of very large clusters at high redshift, the objects which have the more weight in number count analyses, are strongly underestimated.

We provided catalogues of WL calibrated masses corrected for biases and selection effects that cover considerable mass and redshift ranges. We associated mass estimates to the redMaPPer clusters, which were not present in the original catalogue, and we corrected the *Planck* or MCXC masses for the hydrostatic bias. The estimated error budget of the forecasted masses includes uncertainties associated with the proxy measurement, the calibration sample, the scaling relation and the intrinsic scatter, which contributes the most. Errors and biases due to data selection are corrected for. Still, the statistical error is not to be confused with the intrinsic scatter of the scaling relation. In the CoMaLit approach, we modelled the true masses as unscattered and perfectly fitting the scaling relation. It is the WL mass associated with the cluster that is a scattered realization of the true mass.

The next step in mass prediction is the application of scaling relations generalized to include the dependence upon two or more independent observables (Ettori et al. 2012). Ettori (2013) showed that a generalized relation $M \propto L_X^\alpha M_g^\beta T_X^\gamma$, where L_X and T_X are the X-ray luminosity and temperature, respectively, and M_g is the gas mass, can significantly reduce the intrinsic scatter on both galaxy group and cluster scales.

ACKNOWLEDGEMENTS

MS thanks J.-B. Melin and E. Rozo for useful explanations. MS and SE acknowledge the financial contribution from contracts ASI-INAF I/009/10/0, PRIN-INAF 2012 ‘A unique data set to address the most compelling open questions about X-Ray Galaxy Clusters’, and PRIN-INAF 2014 ‘Glittering Kaleidoscopes in the sky: the multifaceted nature and role of galaxy clusters’. This research has made use of NASA’s Astrophysics Data System (ADS) and of the NASA/IPAC Extragalactic Database (NED), which is operated by the Jet Propulsion Laboratory, California Institute of Technology, under contract with the National Aeronautics and Space Administration.

REFERENCES

Andreon S., Bergé J., 2012, *A&A*, 547, A117
 Angulo R. E., Springel V., White S. D. M., Jenkins A., Baugh C. M., Frenk C. S., 2012, *MNRAS*, 426, 2046
 Applegate D. E. et al., 2014, *MNRAS*, 439, 48
 Arnaud M., Pratt G. W., Piffaretti R., Böhringer H., Croston J. H., Pointecouteau E., 2010, *A&A*, 517, A92
 Battaglia N., Bond J. R., Pfrommer C., Sievers J. L., 2012, *ApJ*, 758, 74
 Battaglia N. et al., 2016, *J. Cosmol. Astropart. Phys.*, 8, 013
 Becker M. R., Kravtsov A. V., 2011, *ApJ*, 740, 25
 Bhattacharya S., Habib S., Heitmann K., Vikhlinin A., 2013, *ApJ*, 766, 32
 Butkevich A. G., Berdyugin A. V., Teerikorpi P., 2005, *MNRAS*, 362, 321
 Cypriano E. S., Sodré L., Jr, Kneib J.-P., Campusano L. E., 2004, *ApJ*, 613, 95
 D’Agostini G., 2005, preprint ([arXiv:physics/0511182](https://arxiv.org/abs/physics/0511182))
 Dutton A. A., Macciò A. V., 2014, *MNRAS*, 441, 3359
 Eddington A. S., 1913, *MNRAS*, 73, 359
 Eddington A. S., 1914, *Stellar Movements and the Structure of the Universe*. Macmillan, London
 Eddington A. S., 1940, *MNRAS*, 100, 354
 Ettori S., 2013, *MNRAS*, 435, 1265
 Ettori S., 2015, *MNRAS*, 446, 2629

Ettori S., Rasia E., Fabjan D., Borgani S., Dolag K., 2012, *MNRAS*, 420, 2058
 Fabjan D., Borgani S., Rasia E., Bonafede A., Dolag K., Murante G., Tornatore L., 2011, *MNRAS*, 416, 801
 Farahi A., Evrard A. E., Rozo E., Rykoff E. S., Wechsler R. H., 2016, *MNRAS*, 460, 3900
 Gardini A., Rasia E., Mazzotta P., Tormen G., De Grandi S., Moscardini L., 2004, *MNRAS*, 351, 505
 Giodini S., Lovisari L., Pointecouteau E., Ettori S., Reiprich T. H., Hoekstra H., 2013, *Space Sci. Rev.*, 177, 247
 Gott J. R., III, Vogeley M. S., Podariu S., Ratna B., 2001, *ApJ*, 549, 1
 Gruen D. et al., 2014, *MNRAS*, 442, 1507
 Hoekstra H., Herbonnet R., Muzzin A., Babul A., Mahdavi A., Viola M., Cacciato M., 2015, *MNRAS*, 449, 685
 Hu W., Kravtsov A. V., 2003, *ApJ*, 584, 702
 Jeffreys H., 1938, *MNRAS*, 98, 190
 Kaiser N., 1986, *MNRAS*, 222, 323
 Kay S. T., Peel M. W., Short C. J., Thomas P. A., Young O. E., Battye R. A., Liddle A. R., Pearce F. R., 2012, *MNRAS*, 422, 1999
 Kelly B. C., 2007, *ApJ*, 665, 1489
 Kravtsov A. V., Vikhlinin A., Nagai D., 2006, *ApJ*, 650, 128
 Laureijs R. et al., 2011, preprint ([arXiv:1110.3193](https://arxiv.org/abs/1110.3193))
 Limousin M., Morandi A., Sereno M., Meneghetti M., Ettori S., Bartelmann M., Verdugo T., 2013, *Space Sci. Rev.*, 177, 155
 Malmquist K. G., 1920, *Lund Medd. Ser. II*, 22, 1
 Malmquist K. G., 1922, *Lund Medd. Ser. I*, 100, 1
 Mantz A. B., 2016, *MNRAS*, 457, 1279
 Maughan B. J., 2007, *ApJ*, 668, 772
 Maughan B. J., 2014, *MNRAS*, 437, 1171
 Maughan B. J., Giles P. A., Randall S. W., Jones C., Forman W. R., 2012, *MNRAS*, 421, 1583
 Meneghetti M., Rasia E., Merten J., Bellagamba F., Ettori S., Mazzotta P., Dolag K., Marri S., 2010, *A&A*, 514, A93
 Oguri M., Bayliss M. B., Dahle H., Sharon K., Gladders M. D., Natarajan P., Hennawi J. F., Koester B. P., 2012, *MNRAS*, 420, 3213
 Okabe N., Smith G. P., 2016, *MNRAS*, 461, 3794
 Pierre M. et al., 2016, *A&A*, 592, A1
 Piffaretti R., Arnaud M., Pratt G. W., Pointecouteau E., Melin J.-B., 2011, *A&A*, 534, A109
 Planck Collaboration XX, 2014, *A&A*, 571, A20
 Planck Collaboration XXVII, 2016a, *A&A*, 594, A27
 Planck Collaboration XIII, 2016b, *A&A*, 594, A13
 Planck Collaboration XXIV, 2016c, *A&A*, 594, A24
 Rasia E. et al., 2012, *New J. Phys.*, 14, 055018
 Rines K., Geller M. J., Diaferio A., Kurtz M. J., 2013, *ApJ*, 767, 15
 Rykoff E. S. et al., 2014, *ApJ*, 785, 104
 Saro A., Mohr J. J., Bazin G., Dolag K., 2013, *ApJ*, 772, 47
 Sereno M., 2015, *MNRAS*, 450, 3665
 Sereno M., 2016, *MNRAS*, 455, 2149
 Sereno M., Ettori S., 2015a, *MNRAS*, 450, 3675
 Sereno M., Ettori S., 2015b, *MNRAS*, 450, 3633
 Sereno M., Ettori S., Moscardini L., 2015, *MNRAS*, 450, 3649
 Simet M., Battaglia N., Mandelbaum R., Seljak U., 2017a, *MNRAS*, 466, 3663
 Simet M., McClintock T., Mandelbaum R., Rozo E., Rykoff E., Sheldon E., Wechsler R. H., 2017b, *MNRAS*, 466, 3103
 Smith G. P. et al., 2016, *MNRAS*, 456, L74
 Stanek R., Rasia E., Evrard A. E., Pearce F., Gazzola L., 2010, *ApJ*, 715, 1508
 Svensmark J., Wojtak R., Hansen S. H., 2015, *MNRAS*, 448, 1644
 Teerikorpi P., 1997, *ARA&A*, 35, 101
 Umetsu K., Zitrin A., Gruen D., Merten J., Donahue M., Postman M., 2016, *ApJ*, 821, 116
 Vikhlinin A. et al., 2009, *ApJ*, 692, 1033
 Voit G. M., 2005, *Rev. Modern Phys.*, 77, 207
 von der Linden A. et al., 2014, *MNRAS*, 443, 1973
 Wen Z. L., Han J. L., 2015, *ApJ*, 807, 178
 Wen Z. L., Han J. L., Liu F. S., 2012, *ApJS*, 199, 34

SUPPORTING INFORMATION

Supplementary data are available at [MNRAS](https://www.mnras.org/onlineonly) online.

redmapper_dr8_public_v6.3_MWLc.dat
mcxc_MWLc.dat
HFI_PCCS_SZ-MMF3_R2.08_MWLc.dat

Please note: Oxford University Press is not responsible for the content or functionality of any supporting materials supplied by the authors. Any queries (other than missing material) should be directed to the corresponding author for the article.

APPENDIX: IMPLEMENTATION

The mass forecasting was performed with the package `LIRA`. Let $x, y, \delta x, \delta y, \delta_{xy}$ and z be the vectors storing the values of $x, y, \delta x, \delta y, \delta_{xy}$ and z , respectively. If not stated otherwise, priors are set to the default distributions.

(i) For the mass forecasting of the *Planck* clusters in Section 6.3, we corrected for the distance-dependent Malmquist bias by assigning the selection thresholds in the SZ signal, x_{th} . No error was associated with the thresholds. The analysis was performed with the command

```
> mcmc <- lira(x, y, delta.x=delta.x,
delta.y=delta.y, x.threshold=x.threshold,
z=z, distance='luminosity',
gamma.sigma.Z.Fz='dt', Y.monitored=TRUE,
X.monitored=TRUE, YZ.monitored=TRUE),
```

where the covariate distribution is modelled as a redshift-evolving Gaussian function. On the top of the default values, we also allowed for redshift evolution of the width of the distribution (`gamma.sigma.Z.Fz='dt'`).

Thanks to the options `YZ.monitored=TRUE`, `Y.monitored=TRUE` and `X.monitored=TRUE`, we can monitor the WLC calibrated masses, the WL masses and the covariate X , respectively.

(ii) The forecasting in Section 7 for the redMaPPer catalogue was performed with

```
> mcmc <- lira(x, y, delta.x=delta.x,
delta.y=delta.y, x.threshold=x.threshold,
z=z, distance='luminosity',
gamma.sigma.Z.Fz='dt', mu.Z.min.0=x.min,
sigma.Z.min.0='dunif(10^-6, 0.3)',
Y.monitored=TRUE, X.monitored=TRUE,
YZ.monitored=TRUE),
```

where we corrected for the distance-dependent Malmquist bias by assigning the selection thresholds for each point (`x.threshold`). As covariate distribution, we used a redshift-evolving Gaussian function truncated at small values with a complementary error function centred on `mu.Z.min.0=x.min` and with dispersion `sigma.Z.min.0`. Here, the parameter `x.min` is fixed to the logarithm of the minimum observed richness.

(iii) The forecasting in Section 8 for the MCXC catalogue was performed with

```
> mcmc <- lira(x, y, delta.x=delta.x,
delta.y=delta.y, z=z, distance='luminosity',
gamma.sigma.Z.Fz='dt', Y.monitored=TRUE,
X.monitored=TRUE, YZ.monitored=TRUE),
```

where we could not correct for the distance-dependent Malmquist bias and we modelled the covariate distribution as a redshift-evolving Gaussian function.

Further examples and catalogues can be found at <http://pico.bo.astro.it/~sereno/LIRA/>.

This paper has been typeset from a \LaTeX file prepared by the author.